Science Signaling
AAAS

www.sciencesignaling.org/cgi/content/full/7/316/ra23/DC1

Supplementary Materials for

Intra- and Interdimeric Caspase-8 Self-Cleavage Controls Strength and Timing of CD95-Induced Apoptosis

Stefan M. Kallenberger, Joël Beaudouin, Juliane Claus, Carmen Fischer, Peter K. Sorger, Stefan Legewie, Roland Eils*

*Corresponding author. E-mail: r.eils@dkfz.de

Published 11 March 2014, *Sci. Signal.* **7**, ra23 (2014)
DOI: 10.1126/scisignal.2004738

This PDF file includes:

Other Supplementary Material for this manuscript includes the following:
(available at www.sciencesignaling.org/cgi/content/full/7/316/ra23/DC1)

Caspase-8 model MatLab scripts (zip file of .m files)
Caspase-8 model SBML files (zip file of .xml files)
Caspase-8 single-cell data (Excel)

Text S1: Data Analysis

Quantification of caspase-8 enzymatic activities in single cells

We employed caspase-8 cleavage probes to analyze apoptosis signaling at the single-cell level and generate single-cell data for model fitting. The degree of probe cleavage reflects the integrated activity of caspase-8 over time, but not the caspase-8 activity at a certain time point. We used a simple mathematical model to extract a time course of caspase-8 activity from the probe cleavage data.

The model assumes that enzyme saturation in caspase-8 mediated probe cleavage can be neglected. The cleavage rate of a probe is then proportional to the concentration of the uncleaved probe $[PrF]$ and of caspase-8 $[C8]$ multiplied by the kinetic constant k_{probe}

$$[\dot{Pr}] = k_{probe}[C8][PrF] \Leftrightarrow k_{probe}[C8] = \frac{[\dot{Pr}]}{[PrF]}. \quad (1)$$

The caspase-8 activity profile can thus be calculated by extracting $[\dot{Pr}]$ and $[PrF]$ from the data. In the following, we will express $[\dot{Pr}]$ and $[PrF]$ functions of the average probe intensities in the nucleus I_{ncl} and in the total cell I_{tot}, because these intensities can be extracted most reliably from single-cell measurements.

Upon stimulation, the number of uncleaved probes N_{PrF} is processed to N_{Pr} cleaved probe molecules and $N_F = N_{Pr}$ fluorescent protein molecules. The fluorescence intensity in the nucleus $I_{ncl} = cN_F/V_c$ reflects the number of fluorescent protein molecules N_F in the cell volume V_C, multiplied by a scaling factor c. The total concentration of cleaved probes $[Pr]$ is higher than the concentration of fluorescent protein molecules by the ratio of the cytoplasmic volume V_{cpl} and the total cellular volume

$$[Pr] = \frac{N_{Pr}}{V_{cpl}} = \frac{N_F}{V_{cpl}} = \frac{V_c}{cV_{cpl}} I_{ncl}. \quad (2)$$

The concentration of the uncleaved probes $[PrF]$ can be determined by measuring the average intensity inside the whole cell $I_{tot} = c(N_{PrF} + N_F)/V_c$ as

$$[PrF] = \frac{N_{PrF}}{V_{cpl}} = \frac{V_c}{cV_{cpl}}(I_{tot} - I_{ncl}). \quad (3)$$

Thereby, estimates of the amount of active caspase-8 multiplied by the cleavage constant

$$k_{probe}[C8] = \frac{\dot{I}_{ncl}}{I_{tot} - I_{ncl}} \tag{4}$$

are obtained, eliminating the scaling factor.

The ER-anchored cleavage probe $Pr_{ER}F_1$ can only be accessed by soluble, cytoplasmic caspase-8. Based on the approach described in equations 1-4, we can calculate the activity from cytoplasmic caspase-8 $C8_{cpl}$

$$[\dot{P}r_{ER}] = k_{probe}[C8_{cpl}][Pr_{ER}F_1] \quad \Leftrightarrow \quad k_{probe}[C8_{cpl}] = \frac{\dot{I}_{1,ncl}}{I_{1,tot} - I_{1,ncl}}. \tag{5}$$

The amount of membrane-bound caspase-8 $C8_{mem}$ cannot be calculated directly, because no membrane-specific cleavage probe is available. We consider that the total amount of active casepase-8 equals the sum of soluble and membrane-bound forms ($C8_{tot} = C8_{mem} + C8_{cpl}$), and calculate the membrane-bound activity on the basis of the difference between terms for cytosolic and ER probe cleavage ($Pr_{cpl}F_2$ and $Pr_{ER}F_1$, respectively)

$$\begin{aligned}[\dot{P}r_{cpl}] &= k_{probe}([C8_{mem}] + [C8_{cpl}])[Pr_{cpl}F_2] \quad \Leftrightarrow \\ k_{probe}[C8_{mem}] &= \frac{\dot{I}_{2,ncl}}{I_{2,tot} - I_{2,ncl}} - \frac{\dot{I}_{1,ncl}}{I_{1,tot} - I_{1,ncl}} \quad .\end{aligned} \tag{6}$$

In the case of our experiment F_1 is mGFP and F_2 is mCherry. Automated image analysis was employed to estimate amounts of cleaved and uncleaved probes. The total cellular and the nuclear fluorescence intensities were extracted by segmentation. As described by equations 1-6, slopes of nuclear fluorescence intensities had to be estimated to calculate caspase-8 cleavage activities. To improve the robustness of our slope estimation, temporal derivatives in equations (5) and (6) were calculated over longer time intervals, in which several intensity measurements were averaged. For each cell, caspase-8 activity values were calculated in eight equidistant time intervals. We choose this relatively small number to obtain a reasonable signal-to-noise ratio in p43 and p18 activities, which limited the propagated error from noisy intensity measurements. Optimizing model fitting performance was a further reason to keep the number of data points for each cell low.

Smoothing splines were fit to the nuclear intensity trajectories. The errors $\Delta I_{1,ncl}$ and $\Delta I_{2,ncl}$ were estimated as the standard deviation of the difference between the smoothing spline and the experimental data. For $I_{1,tot}$ and $I_{2,tot}$ an error of 10 percent was assumed. Figure S3 shows trajectories of estimated total caspase-8 activities in single CD95-HeLa and wild-type HeLa cells. In a few cells, almost the total amount of cytoplasmic cleavage probes was cleaved before apoptosis. In this case, the nuclear fluorescence intensity approximates I_{tot}. When the difference between I_{tot} and I_{ncl} becomes small, cleavage activities cannot be accurately extracted by equations (5) and (6). Therefore, we stopped

calculating caspase-8 activities when the nuclear intensity I_{ncl} was equal or larger than 90% of the average intensity of the whole cell $I_{ncl} \geq 0.9 \cdot I_{tot}$. When caspase-8 activities were calculated beyond this limit, the trajectories flattened due to probe depletion.

Comparison of caspase-8 activity profiles in FRET- and NES-probe measurements

Currently, two methods are available to monitor caspase-8 activity in single cells. Several studies used FRET-reporters that consist of a pair of fluorescent proteins, usually CFP and YFP, connected with a cleavage sequence that is specific for caspase-8 (29, 49, 50). We established a different method to investigate the spatiotemporal cleavage activity of caspases (19) based on multiple localization probes that contain a subcellular compartment anchor, a cleavage site, and a fluorescent protein. The NES probe designed to indicate the cleavage activity inside the cytoplasm contains a nuclear export sequence (NES). Therefore, the uncleaved probe is actively carried out of the nucleus and is restricted to the cytoplasmic volume (19). After cleavage, the fluorescent protein can enter the nucleus while the residual NES part remains in the cytosol. By measuring the fluorescence intensity inside the nucleus, the concentrations of the cleaved and the non-cleaved probes can be estimated. Here, we compared both methods. Figure S4A shows microscopic image data from exemplary cells that after transient transfection simultaneously express the FRET and NES cleavage probes and were stimulated with CD95L. Cleavage of the NES probe containing the cleavage site for BID (top panel, NES-ELQTDG-mCherry) can be measured by an increase of the nuclear fluorescence intensity $I_{mCherry,ncl}$, whereas the FRET probe (CFP-ELQTDG-YFP) cleavage is indicated by an increase of the I_{CFP} / I_{YFP} ratio (bottom panel). The single cell trajectories of cells that simultaneously express both probes showed high correlation coefficients (fig. S4B-S4D), indicating that the two methods produce comparable results.

Quantification of total signaling protein concentrations

We determined absolute signaling protein concentrations and their variability by quantitative Western blotting and flow cytometry-based assays to further constrain our mathematical model of caspase-8 processing.

Estimates of average protein amounts of FADD, procaspase-8, and BID in probe-expressing cells were obtained by calibrated Western blots (table S4). We generated cell lines stably expressing FADD-GFP or p55-GFP from wild-type HeLa cells, and transiently expressed BID-GFP-mCherry in wild-type HeLa cells. FADD-GFP, p55-GFP, and BID-GFP-mCherry concentrations in fusion protein lysates were estimated by simultaneously blotting fusion protein lysates together with different doses of recombinant GFP. Endogenous amounts of FADD, p55, BID, and cytosolic cleavage probes (NES-GIETDS-mCherry) were determined by blotting different doses of fusion protein lysates together with lysates of probe expressing CD95-HeLa and wild-type HeLa cells (fig. S9-S11, table S4). For estimations of ER probe (Calnexin-GIETDS-mGFP) concentrations, lysates of probe-expressing cell lines were blotted together with recombinant GFP (fig. S11). Concentrations of FADD and p55 were estimated in an earlier study for CD95-HeLa and wild-type HeLa cells (25). Here, we found FADD and p55 concentrations of similar magnitude in probe-expressing CD95-HeLa and wild-type HeLa cells.

Using flow cytometry to estimate CD95R numbers and set upper and lower boundaries for initial concentrations

We determined average numbers of CD95Rs and variability of CD95Rs, FADD, p55, and BID in stably probe-expressing or nontransfected wild-type HeLa and CD95-HeLa cells by immunostaining followed by flow cytometry (fig. S12 and S13, tables S5 and S6). The absolute concentration of CD95Rs was estimated from calibration beads carrying defined epitope numbers for secondary antibodies (table S5, fig. S12). FACS distributions were used to restrict the variability of initial protein concentrations in the model to physiologically reasonable amounts. To measure variability of protein amounts independently from cell size, we filtered for cells of similar volumes by gating for narrow front scatter and side scatter intervals. As controls in FACS measurements, cells were treated with secondary but no primary antibodies. To correct intensity measurements for background fluorescence, medians of normal distribution function fits to intensities of control measurements were subtracted. We determined the lognormal distribution parameters σ_{CD95R}, σ_{FADD}, σ_{p55}, and σ_{BID} for initial concentration distributions by fitting to rescaled and background-corrected FACS signals. We obtained coefficients of variation of protein concentrations in the range of 0.8 to 1.1, which are rather large compared to studies on the variability of single-cell protein amounts (51, 52) and are probably due to additional variability from intracellular antibody staining and FACS measurements. To restrict initial protein concentrations in the model, 5% and 95% percentiles of the concentration distributions measured by FACS were calculated and combined with mean signals from Western blots to set the lower and upper limits for parameter fitting, respectively (table S6).

Cellular volumes that were used to calculate average protein concentrations from protein numbers per cell and surface areas were determined by segmentation from confocal microscopic image stacks (table S7).

Text S2: Model implementation and fitting

Model of receptor oligomerization and activation

We observed that caspase-8 activation and cell death induction occur with fast kinetics at intermediate ligand concentrations and were slower upon weak and very strong stimulation (Fig. 2 and fig. S3). In the following, we derive a simple mathematical model of receptor oligomerization that shows an inverse bell-shaped dose-response curve, thereby explaining particularly fast signaling kinetics at intermediate ligand concentrations.

The inverse bell-shaped cell death kinetics can be explained by the binding of a multivalent cell death ligand to monovalent cell death receptors (Fig. 2B). The model is based on the following three premises. (i) CD95 receptors oligomerize and may exist as pre-formed oligomers in the absence of stimulation (53–55). (ii) Only oligomerized receptors bound to extracellular ligand are biologically active and serve as a platform for procaspase-8 activation. (iii) The T4-CD95 ligand used in this study is a pure and stable trimer (26) that efficiently induces receptor oligomerization by simultaneously binding to three receptor monomers (56–59). These features of receptor signaling are sufficient to explain the inverse bell-shaped dose-response profile: Each monomeric receptor binds with 1:1 stoichiometry to a trimeric ligand if the ligand is in large excess over the receptors. The system is thus shifted towards biologically inactive one-to-one complexes of receptors and ligands upon strong stimulation, whereas intermediate concentrations of the trimeric ligand efficiently oligomerize and activate the receptor.

The assembly of active death receptor complexes occurs within a few minutes after ligand addition (1) and is a rapid process compared to caspase-8 activation. We, therefore, applied time scale separation of both processes and assumed that the receptor-ligand binding was at steady state for mathematical modeling. Below, we derive an analytic expression describing steady-state concentration of active receptors that is dependent on the total receptor concentration and the cell death ligand concentration.

The overall concentration of receptors R_{tot} consists of receptor/ligand complexes $R_{L,tot}$ and free receptors

$$R_{F,tot} = R_{tot} - R_{L,tot}. \tag{7}$$

Active receptors are denoted as R^*. The steady-state concentration of receptor/ligand complexes $R_{L,tot}$ depends on the ligand concentration L and the ligand dissociation constant K_{DL}

$$K_{DL} = \frac{k_{L,off}}{k_{L,on}} = \frac{R_{F,tot} L}{R_{L,tot}} \tag{8}$$

with kinetic constants $k_{L,on}$ for binding and $k_{L,off}$ for unbinding, assuming the same binding kinetics for different receptor oligomerization states. Including Equation 7 yields

$$R_{L,tot} = R_{tot} \frac{L}{L + K_{DL}}. \quad (9)$$

Solving the steady-state equation for binding of two free receptors to the part of inactive receptor/ligand complexes $R_{L,tot} - R^*$ with the receptor dissociation constant K_{DR},

$$0 = (R_{L,tot} - R^*) {R_{F,tot}}^2 - K_{DR} R^*$$

applying equations (7) and (9) yields

$$R^* = \frac{{R_{tot}}^3 L {K_{DL}}^2}{(L + K_{DL})({R_{tot}}^2 {K_{DL}}^2 + K_{DR} L^2 + 2 K_{DR} L K_{DL} + K_{DR} {K_{DL}}^2)}. \quad (10)$$

We implemented Equation 10 to calculate the amount of active receptors R^* at the beginning of each parameter optimization step in our full model that takes into account caspase-8 autoprocessing (see below). The initial concentration of receptors R_{tot} and the constants K_{DL} and K_{DR} at given L were estimated by model fitting to experimental data. The association of active receptors with FADD and subsequent reaction steps were assumed to be slow compared to receptor-ligand binding and thus implemented as ODEs.

Model variants of caspase-8 activation

We employed mass-action based ODEs to describe caspase-8 autoprocessing. The previously derived algebraic receptor activation model served as the input for the caspase-8 autoprocessing model. Reactions in the caspase-8 autoprocessing model include FADD and p55 binding to active receptors and subsequent processing of receptor-associated p55 to fully cleaved p18, either through the p43 or the p30 intermediates (Fig. 3B, fig. S6). Because c-FLIP molecule numbers were in the range of a few hundred and procaspase-8 molecule numbers were in the range of ~$3 \cdot 10^5$ per cell, which is below the relative proportions in which c-FLIP regulates caspase-8 activation (25), we did not include c-FLIP in our kinetic models. Intra- and interdimeric modes of caspase-8 autoprocessing could be discriminated by fitting different model variants (Fig. 3B, fig. S6B) to experimental data. The model variants differ in the cleavage kinetics of the caspase-8 autoprocessing reactions: Cis cleavage reactions are represented by a unimolecular reaction, whereas trans cleavage reactions are represented by a bimolecular reaction.

To avoid combinatorial complexity, we made several assumptions for describing the dimer dynamics using a simplified reaction scheme with monomeric reaction steps (fig. S6). We assumed that FADD and p55 binding are highly cooperative processes. Cooperativity implies that a second p55 or FADD monomer rapidly binds to the receptor complex, once the first monomer has been recruited. This cooperativity means that binding of two monomers is mechanistically equivalent to one bimolecular reaction thus can be described by a single reaction step.

Procaspase-8 needs to bind in a dimeric configuration to death receptors to be capable of autoprocessing. We did not explicitly distinguish between different homo- and heterodimeric

configurations of caspase-8 at the DISC, and instead described the behavior of p55, p43, p30, and p18 monomers in the dimers. This is justified when assuming that the cleavage activity of a procaspase-8 dimer is independent of the respective dimer partner molecule. This implies, for example, that the activity of p43 in p43-p43 homodimers contributes to the catalytic activity of the model species p43 to the same extent as p43 in the heterodimers (p55-p43, p30-p43).

The subsequent caspase-8 autoprocessing occurs at five cleavage sites, two of which are located in the enzymatic domain of procaspase-8 (Asp^{374} and Asp^{384}), whereas the remaining ones lie between the prodomain and the enzymatic domain (Asp^{210}, Asp^{216}, and Asp^{223}) (11, 27). These groups of neighboring cleavage sites are located in close vicinity, suggesting that the corresponding cleavage products show similar biological activity. We, therefore, assumed in the model that caspase-8 autoprocessing involves only two cleavage events, one between the prodomain and the enzymatic domain (p55 to p30, p43 to p18), and one between the enzymatic subdomains (p55 to p43, p30 to p18) (fig. S1). The kinetic parameters for each cleavage reaction can be regarded as collective parameters for any prodomain site or enzymatic site cleavage, respectively.

The prodomain of procaspase-8 allows for high-affinity binding to the FADD-receptor complex. The species p55 and p43 contain the prodomain and are assumed to be associated with the receptor complex (11). We neglected unbinding of these species, assuming that unbinding is slow compared to the subsequent cleavage reactions. The prodomain is absent from p18 and p30, suggesting that these species can dissociate from the receptor complex and diffuse into the cytosol. We assume in the model that p18 is immediately released from the DISC, because only weak traces of p18 are measured in DISC immunoprecipitates (11). We assume that the p30 intermediate is retained at the DISC in the model, because it is only transiently formed in little amounts. Thus, the majority of p30 is expected to form heterodimers with p55 or p43 and therefore remain bound to the DISC through the dimer interface. Probe cleavage was implemented as described above and BID cleavage was modeled like the NES probe cleavage.

Linking single-cell and population observables

Our experimental data set comprised measurements at the single-cell and population levels. Single-cell models were directly fitted to single-cell measurements, and variability was introduced by allowing the initial signaling protein concentrations to vary between individual cells. Population-based measurements were represented in the model by summing up over the trajectories of multiple single-cell models. In the following, we describe in detail how model variables were fitted to experimental data.

Single-cell measurements $\vec{y}_n$ of n cells for the uncleaved probe concentrations, $y_{Pr_{ER}F_1}$ and $y_{Pr_{cpl}F_2}$, as well as measurements for effective caspase-8 concentrations y_{p43} and y_{p18} were used for model fitting. The model variables x were linked to measurements using scaling factors that were estimated from the data. Ten cells exposed to each of four different ligand concentrations were included; thus data from 80 cells was included. When fitting a model topology to data from 80 cells, more than 2560 residuals were minimized (80 cells x 4 observables x 8 time points), which resulted in a duration of approximately 20 minutes for one fit on a cluster node.

To include population data into the parameter-fitting procedure and link population data with model variables for single cells, population observables Y were introduced. A population observable was assumed to be proportional to the sum of the corresponding single-cell variables x_n, weighted by the cellular volumes V_n that were determined from segmented microscopic data. The total amount of caspase-8 and BID, estimated from the band intensities, did not substantively change over time. Each caspase-8 species and the two forms of BID were normalized by the respective total concentration to obtain estimates for the percent cleavage at every time point and then these ratios were used for model fitting. Single-cell observables

$$\vec{y}_n(t_i) = \begin{pmatrix} s_{C8}[p43]_n(t_i) \\ s_{C8}[p18]_n(t_i) \\ s_{F1}[Pr_{ER}F_1]_n(t_i) \\ s_{F2}[Pr_{cpl}F_2]_n(t_i) \end{pmatrix}$$

of cells with volumes V_n with scaling factors s were simultaneously used with population observables

$$Y(t_j) = \begin{pmatrix} I_{p55}(t_j)/I_{C8,tot}(t_j) \\ I_{p43}(t_j)/I_{C8,tot}(t_j) \\ I_{p30}(t_j)/I_{C8,tot}(t_j) \\ I_{p18}(t_j)/I_{C8,tot}(t_j) \\ I_{BID}(t_j)/I_{BID,tot}(t_j) \\ I_{tBID}(t_j)/I_{BID,tot}(t_j) \end{pmatrix} = \begin{pmatrix} \sum_n V_n\left([p55]_n(t_j) + [DISCp55]_n(t_j)\right)/S_{C8} \\ \sum_n V_n[p43]_n(t_j)/S_{C8} \\ \sum_n V_n[p30]_n(t_j)/S_{C8} \\ \sum_n V_n\left([p18]_n(t_j) + [p18i]_n(t_j)\right)/S_{C8} \\ \sum_n V_n[BID]_n(t_j)/S_{BID} \\ \sum_n V_n[tBID]_n(t_j)/S_{BID} \end{pmatrix}.$$

We avoided introducing another scaling factor by using Western blot band intensity fractions. Western blot band intensities were normalized to the sums of caspase-8 or BID intensities

$I_{C8,tot} = I_{p55} + I_{p43} + I_{p30} + I_{p18}$, and

$I_{BID,tot} = I_{BID} + I_{tBID}$,

to achieve a better signal-to-noise ratio and to obtain a direct relation to the corresponding sums of single-cell variables that were normalized with

$S_{C8} = \sum_n V_n\left([p55]_n + [DISCp55]_n + [p43]_n + [p18]_n + [p18i]_n\right)$, or

$S_{BID} = \sum_n V_n\left([BID]_n + [tBID]_n\right)$.

Models with different prodomain site cleavage constants for p55 and p43 have only slight improvements in fit quality

In the initial formulation of the 'cis/cis' model variant, we assumed a single kinetic constant for both prodomain cleavage reactions (p55 to p30, p43 to p18) and one for enzymatic domain cleavage reactions (p55 to p43, p30 to p18). The inability of this model to fit the data may be due to an oversimplification: Faster cis prodomain cleavage from p43 to p18 than from p55 to p30 may be expected, because the active center of p43 is constantly open after cleavage of the enzymatic domain. We, therefore, implemented an extended 'cis/cis' variant with two different prodomain cleavage parameters for the reactions from p55 to p30 and from p43 to p18, and assessed its ability to fit the data. However, this model extension did not improve fit quality (fig. S14). Therefore, a cis-only model topology with separate cleavage constants for the two prodomain cleavage reactions is not capable of explaining the experimental data.

Text S3: Model analysis and verification

Caspase-8 cleavage dynamics in fits of different model variants

The minimal 'cis/trans' model and more complex variants fitted the data equally well, suggesting that the 'cis/trans' mechanism is sufficient to explain the experimental observations. In the following, we analyze reaction fluxes in the models to show that the best-fit parameter sets of complex model variants behave similarly to the minimal 'cis/trans' model. Our analysis was based on the idea that reactions not considered in the minimal 'cis/trans' model should exhibit negligible flux in more complex variants.

To distinguish between relevant and irrelevant cleavage reactions, we calculated fluxes by multiplying caspase-8 intermediate concentrations with the kinetic rate constants of the reactions they feed into. Starting from model fits of the variant that includes all possible cleavage modes ('cis+trans/cis+trans'), we discarded reactions with small fluxes to reduce the model. Figures 4D-4G and fig. S15-S17 show fluxes for reactions of p55, p43, p30, and p18 for CD95-HeLa and wild-type HeLa cells as a function of time at different ligand concentrations. For each model variant, starting from the median estimated initial concentrations from the best 1% of n=1000 model fits to the full data set (single-cell and population data), reaction fluxes were calculated until the median cell death time (fig. S15-S17). Fractions of the initial p55 concentration that were processed by a certain cleavage reaction (cis cleavage, trans cleavage by p43 or trans cleavage by p55) between ligand addition and the time of apoptosis were calculated (Fig. 4D-4G, fig. S16 and S17). Figures S16C and S17E show comparisons of the estimated half-life times of caspase-8 intermediates between the 'cis+trans/cis+trans', the 'cis/trans' and the 'trans/trans' topologies.

Model fits to the 'cis+trans/cis+trans' variant showed that some cleavage reactions have negligible fluxes only (Fig. 4D-4G). In the best model fits, the largest amount of p55 is processed in trans by p43 to p43, whereas trans cleavage by p55 plays a minor role. Cis fluxes for the enzymatic domain cleavage reactions (p55 to p43, p30 to p18) are negligible. In contrast, for prodomain cleavage reactions (p43 to p18, p55 to p30), fluxes for cis reactions are larger than for trans reactions. As a smaller fraction of procaspase-8 is cleaved at the prodomain site, less p55 is processed through p30 than through p43, especially in CD95-HeLa cells. Thus, in the complete 'cis+trans/cis+trans' topology, the prodomain site is mainly cleaved in cis reactions, whereas trans cleavage reactions have smaller contributions.

This motivates model reduction by rejecting enzymatic domain cis cleavage and prodomain trans cleavage, which results in the 'cis/trans' model. For the less contributing prodomain trans cleavage reactions, larger fluxes are estimated for trans cleavage by p55 than by p43, opposite to the trans cleavage reactions of the enzymatic site, for which p43 has larger trans cleavage activity. Here, trans cleavage of p55 by p55 is more similar to the kinetics of p55 cis cleavage than to the kinetics of p55 trans cleavage by p43. Therefore, it is more difficult to discriminate between cis cleavage of p55 with a reaction rate proportional to [p55] and trans cleavage of p55 by p55 with the reaction rate proportional to $[p55]^2$.

Flux analyses of model fits to the 'cis/trans' variant (fig. S16) show similar characteristics to the full 'cis+trans/cis+trans' topology. Half-lives for p55, p43, p30 and p18 are similar for the two models (fig.

S16C). In comparison to the 'cis/trans' topology, fit quality to experimental data was slightly worse by the 'trans/trans' model in which the prodomain site and the enzymatic domain site are both cleaved in trans. Clear discrimination between these two variants was not possible by model fitting. However, in contrast to the 'cis/trans' model, analysis of reaction fluxes and predicted half-life times for the best fits of the 'trans/trans' model showed a distinctive divergence from predictions of the full 'cis+trans/cis+trans' model and extremely large half-life times for p18, (fig. S17).

Monte Carlo modeling reveals qualitative differences in 'cis/cis' and 'cis/trans' topologies

The model fitting results suggest that trans cleavage is required for caspase-8 activation, but did not provide insights into why the pure cis mechanism fails to fit the data. We systematically compared the fits of the 'cis/cis' and 'cis/trans' models to understand how the two mechanisms differ. We noted that the 'cis/cis' mechanism fails to explain the switch-like accumulation of the catalytically active p43 intermediate observed in single-cell measurements (Fig. 5E). This indicated that trans cleavage may result in a positive feedback loop that amplifies the signal and thereby induces a more rapid caspase-8 activation and cell death.

We performed an exhaustive analysis of the parameter space for 'cis/cis' and 'cis/trans' models to show more rigorously that switch-like caspase-8 activation can only be observed in a 'cis/trans' mechanism. The kinetic parameters of the models were randomly sampled 10^4 times, and simulation runs were performed for each parameter set in a Monte Carlo approach. Kinetic parameters were sampled from uniform distributions within two interval sizes, one for fast binding reactions for Ligand, FADD, and p55 ($k\epsilon[10;10^4]$), and one for slow reactions ($k\epsilon[10^{-3};1]$). Systematic analysis of the simulation results showed that 'cis/cis' and 'cis/trans' models differ in the switch-like behavior of the time courses. In general, 'cis/trans' trajectories show a steeper time course for cytosolic probe cleavage than 'cis/cis' trajectories, especially in CD95-HeLa cells (Fig. 5F). The cytosolic probe cleavage switched from 5% to 50% in a less than two-fold increase in time for the trans mechanism, whereas the temporal switch was generally shallower for the cis simulations.

This complementary approach can further support discrimination between 'cis/cis' and 'cis/trans' topologies by trajectory shape attributes. To this end, we determined the times until 5% or 50% cytosolic probe cleavage to describe two major trajectory characteristics, a delay period of low cleavage activity ($t_{5\%}$) and a period of accelerated cleavage between $t_{5\%}$ and $t_{50\%}$, as indicated in fig. S18A (left plot). Figure S18B shows combinations of the cytosolic probe cleavage times $t_{5\%}$ and $t_{50\%}$ for simulations and experiments that were normalized by mean $t_{5\%}$ of HeLa cells, respectively. To display valid areas of possible $t_{5\%}$ and $t_{50\%}$ combinations for 'cis/cis' and 'cis/trans' models, we calculated dot densities. Areas that contain 99% of the integrated density of simulation results are surrounded by solid lines for the two model variants. Experimental $t_{5\%}$-$t_{50\%}$ combinations for CD95-HeLa cells lie within the valid area for the 'cis/trans', but outside the area for the 'cis/cis' model, which does not support relatively low ratios of $t_{50\%}$ to $t_{5\%}$ (fig. S18B, left plot). In contrast, most of the experimental measures for wild-type HeLa cells lie within valid areas of both topologies (fig. S18B, right plot). Here, as seen from model fitting to single-cell data, CD95-HeLa cells support mechanistic discrimination, whereas for wild-type HeLa cell results both topologies are tolerable. The trajectories are less switch-like in cells with fewer receptors: Comparing

between mean $t_{5\%}$ and $t_{50\%}$ for CD95-HeLa and wild-type HeLa cells ($\hat{t}_{5\%,CD95-HeLa} / \hat{t}_{5\%,HeLa} \approx 0.26$, $\hat{t}_{50\%,HeLa} / \hat{t}_{5\%,HeLa} \approx 2.8$, $\hat{t}_{50\%,CD95-HeLa} / \hat{t}_{5\%,HeLa} \approx 0.46$) shows that tenfold fewer receptors cause a stronger decrease in $t_{50\%}$ (factor of ≈ 6.1) than in $t_{5\%}$ (factor of ≈ 3.8) (fig. S18B).

In conclusion, simulating trajectories from random sets of kinetic parameters and extracting characteristic trajectory shape parameters confirmed that the 'cis/trans' but not the 'cis/cis' model can explain single-cell data from live-cell experiments.

Cleavage probes containing caspase-8 autoprocessing sites support a 'cis/trans' mechanism

Model fitting to single-cell and population data favored trans kinetics for cleavage of the enzymatic domain site and a cis reaction for prodomain site cleavage (Fig. 3D). However, the 'trans/trans' variant, in which both sites are cleaved with trans mechanisms, could not unequivocally be rejected by model fitting to experimental data. We designed cleavage probes containing caspase-8 autoprocessing sites and analyzed their cleavage kinetics to provide independent experimental support for 'cis/trans' cleavage reactions. We reasoned that cleavage probes requiring a bimolecular association with caspase-8 would mimic a trans reaction between caspase-8 dimers.

We expressed cleavage probes that consisted of a myristoylation-palmitoylation (Myr-Palm) domain, a spacer of snap tags, cleavage sequences [MTISDS (caspase-8 prodomain site Asp^{210}), PREQDS (caspase-8 prodomain site Asp^{216}), PVETDS (caspase-8 enzymatic subdomain linker site Asp^{374}), or ELQTDG (BID)], and a fluorescent protein in wild-type HeLa cells. We also expressed cleavage probes that consisted of a nuclear export signal (NES), all prodomain cleavage sites (Asp^{210}, Asp^{216} and Asp^{223}), the sequence DEVA (not cleavable for caspase-8), or ELQTDG (BID), and a fluorescent protein in wild-type HeLa cells as described previously (19). Cells simultaneously expressed probes with the BID cleavage sequence bound to mCherry and probes containing one of the other cleavage sequences bound to YFP. The BID probe cleavage kinetics served as a reference.

After probe cleavage, the fluorescent protein can enter the nucleus; whereas uncleaved probes are exclusively localized at the plasma membrane. After ligand addition, fluorescence intensity in nuclear regions of interest was measured to quantify probe cleavage, similar to the probe cleavage experiments used to generate single-cell data for active caspase-8. Here, we used the leucine zipper-soluble CD95 ligand (LZ-sCD95L) (46) as described in Beaudouin *et al*. (19) to stimulate apoptosis. To compare between groups of signal trajectories, we normalized nuclear intensity trajectories to the time of apoptosis indicated by membrane blebbing and to the average signal of the entire cell (Fig. 5A-5C) or to the saturation limit indicating cleavage of the total amount of probes (Fig. 5D). Average trajectories approximate the value one if the nuclear intensity is equal to the average intensity of the cell.

Whereas the MyrPalm probe containing the enzymatic domain site Asp^{374} is cleaved as efficiently as the MyrPalm-BID probe (Fig. 5D), MyrPalm probes with prodomain sites are hardly cleaved (Fig. 5A-5B). Furthermore, cytosolic NES probes showed that trajectories of probes with all prodomain cleavage sites were similar to trajectories of probes with non-cleavable sites (Fig. 5C). This validates the hypothesis,

that prodomain site cleavage is a cis mechanism within procaspase-8 dimers rather than a trans reaction between neighbored dimers with caspase-8 intermediates.

Sensitivity analysis predicts effects of fold-changes in initial protein concentrations

We tested if the 'cis/trans' model fitted to a test data set from CD95-HeLa cells can predict cell death kinetics and variability of cell death times in wild-type HeLa cells. Within the ensemble of single-cell models cell-to-cell variability was explained by assuming equal kinetic parameters but different initial protein concentrations of CD95, FADD, procaspase-8, and BID (Fig. 6C and 6D).

To predict required conditions for cell death, we fitted an ensemble of 40 single-cell models to a training data set of 40 CD95-HeLa single-cell datasets (10 cells per ligand concentration) combined with Western blot data for caspase-8 intermediates, BID, and tBID, and thereby estimated initial protein concentrations for each cell in the training dataset (Fig. 6B). The trained model was then used to predict the fraction of tBID at the time of cell death. For each cell in the training dataset, the model was integrated, starting at the estimated protein concentration until the time of apoptosis. The predicted tBID concentration at this time was then regarded as the tBID threshold sufficient for apoptosis.

To simulate kinetics of wild-type HeLa cells, we assumed that initial concentrations of all involved signaling proteins, except the CD95 receptor and tBID thresholds, were lognormally distributed and equal between CD95-HeLa and wild-type HeLa cells. To simulate apoptosis in wild-type HeLa cells, a lognormal multivariate distribution was compiled from median FADD, p55, and BID concentrations and median tBID threshold estimates, and the experimentally determined mean CD95R concentration of wild-type HeLa cells. If possible, variances of initial concentration estimates and tBID thresholds in the training data set were taken into account, according to the procedure of previous studies (60). Although covariances between FADD, p55, BID concentrations and tBID thresholds were included, other covariances with CD95R concentration were not. Random vectors of initial concentrations and tBID thresholds were sampled from this distribution, representing simulated conditions of wild-type HeLa cells.

For different ligand concentrations, the model was integrated for 100 randomly chosen sets of initial concentrations and tBID fractions until the respective tBID threshold was reached, which was regarded as time of cell death. Cells, in which tBID thresholds were not reached, were regarded as "survivors." We distinguished between simulated cells, in which tBID thresholds were not reached within the time of the experiment (13 hours) or within the maximal integration time (10^4 minutes).

Regulatory control in signaling networks is often distributed unequally, implying that different signaling species control different aspects of the signaling response. We analyzed how the total cellular concentrations of CD95L, CD95R, FADD, p55, and BID control the cell death kinetics and variability by a systematic sensitivity analysis.

To study functional roles of these proteins, we simulated cell death kinetics at different fold-changes of initial protein concentrations, using the 'cis/trans' model fitted to the complete set of CD95-HeLa and wild-type HeLa data (Fig. 7, fig. S19-S21). From initial protein concentration and tBID threshold estimates, separate lognormal multivariate joint distributions for CD95-HeLa and wild-type HeLa cells were determined, including all variances and covariances between the concentrations of CD95R, FADD, p55, and BID and tBID thresholds. Random vectors were sampled from these distributions and the model was integrated with different fold-changes between 0.1 and 10 times the original concentration, separately for each protein. Equivalent death times were determined by integrating the model until tBID concentrations arrived at required thresholds. Cells, in which tBID thresholds were not reached within the maximum integration time, were considered survivors.

From simulations of 100 random samples for each condition, we determined median cell death times, coefficients of variation of cell death times, and surviving fractions. Additionally, trajectories of surviving fractions of cells with an apoptosis time shorter than the experimental duration of 13 hours ($t_{apt}<t_{exp}$) were calculated, representing fractions of cells that survive the duration of the experiment. Predictions at the ligand concentration of 500 ng/ml are shown in Fig. 7, and predictions at the other experimentally used ligand concentrations, which mostly lead to similar characteristic observations, are shown in fig. S19 and S21.

Cell-to-cell variability and speed of cell death depended on concentrations of the upstream signaling species death ligand, death receptors, and FADD (Fig. 7B and 7C). These species determine the number of active DISCs, which represent the bottleneck in caspase-8 activation especially in wild-type HeLa cells. In CD95-HeLa cells, overexpression of CD95R, FADD, p55, or BID barely influenced cell death variability and reduction down to a fold change of about one third only weakly affected the variability coefficient (Fig. 7C and fig. S19). In contrast to upstream species, the concentrations of the downstream species procaspase-8 and BID had only a minor influence on cell death timing and variability.

Cellular survival, however, was strongly affected by the downstream signaling proteins procaspase-8 and BID, because below a certain concentration, the apoptosis-inducing tBID thresholds were not reached (Fig. 7B and 7C, lower rows). After cleavage of p55 to the active intermediate p43, the active time, during which a caspase-8 molecule can cleave downstream substrates, is limited due to the short half-life of p18. Therefore, after p43 is cleaved into p18 and before p18 is inactivated, only a limited number of substrate molecules can be cleaved. If the initial concentration of p55 is low, its processing through p43 or p30 to the unstable p18 might not allow sufficient active caspase-8 species to accumulate for cleaving BID. Thus, reduction of p55 concentrations in a population increases the amount of surviving cells, in which not enough tBID can be processed by activating the available pool of procaspase-8. The abundance of the CD95R and FADD had less influence on survival fraction, especially in CD95-HeLa cells in which survival was independent from ligand, receptor, and FADD concentrations.

Cell-to-cell variability was influenced by receptor oligomerization. Distributions of active receptor fractions in wild-type HeLa and CD95-HeLa cells were predicted after model fitting (fig. S20). Variability in inverse bell-shaped active receptor profiles can have a pro-survival effect and increases the variability in the time to cell death in a cellular population with variable receptor concentrations. At low receptor

numbers, there are too few receptors to oligomerize and form the DISCs. Increasing ligand concentration towards the saturation concentrations in cells with low receptor numbers enlarges cell death variability: In cells with small numbers of receptors death kinetics are decelerated, whereas in cells with higher numbers of receptors cell death is accelerated.

Additionally, we calculated changes in cell death medians and coefficients of variation due to two-fold changes in initial concentrations at different ligand concentrations (fig. S21). For this purpose, the effects of changing from $1/\sqrt{2}$ to $\sqrt{2}$ times the estimated initial concentrations were determined. For wild-type HeLa cells, the simulations showed that the cell-to-cell variability and the speed of cell death depended on the concentrations of the death ligand, death receptors, and FADD. Due to inverse bell-shaped active receptor profiles, the influence of changing the concentration of the ligand or receptor on cell death timing and variability can be small or large, depending on the initial ligand concentration.

In some contexts, overexpression of an apoptotic signaling protein can increase its influence on cell death variability (60). Here, we see the contrary phenomenon: Receptor overexpression causes the cell death variability of CD95-HeLa cells to be less sensitive to CD95R concentration changes.

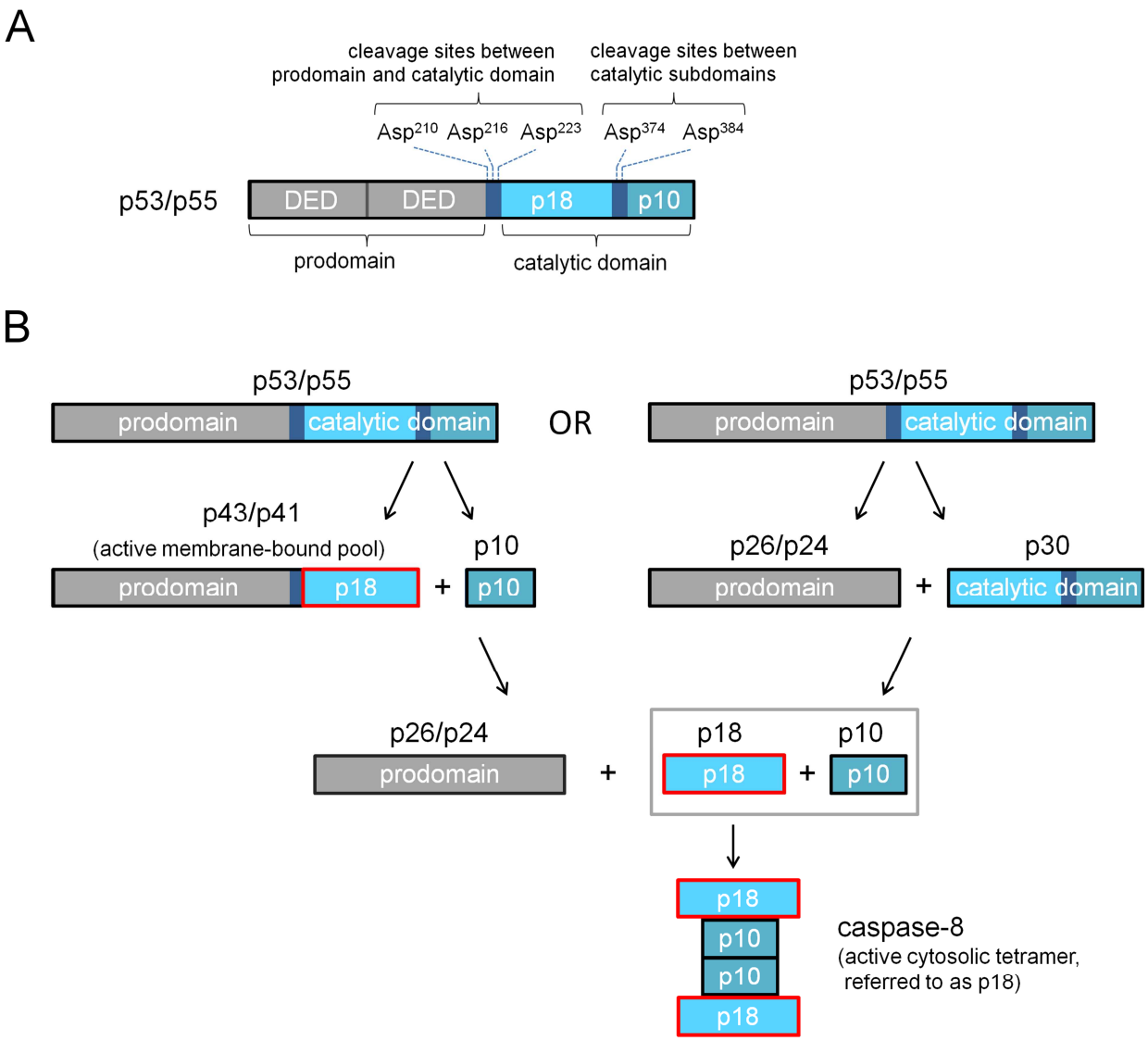

Figure S1. Procaspase-8 and its cleavage products. To form mature caspase-8, the isoforms procaspase-8a/b (p53/p55) can be either cleaved after aspartate residues between the enzymatic subdomains to p43/p41 and p10 or between the prodomain and enzymatic domain to p30 and p26/p24. Further cleavage of either p43 or p30 generates the fragments p18 and p10. Two cleavage products, p43 and p18, can cleave downstream substrates of caspase-8. While the cleavage activity of DISC-bound p43 is restricted to the plasma membrane, p18 enters the cytosol. Active cytosolic caspase-8 is exists as $(p18)_2(p10)_2$ hetero-tetramers. (**A**) A schematic of the cleavage sites and and subdomains in procaspase-8. (**B**) A diagram showing the two pathways through which the final products p24/p24, p18, and p10 can be generated and highlighting the active forms in red. Colors in B correspond to those in Fig. 1A.

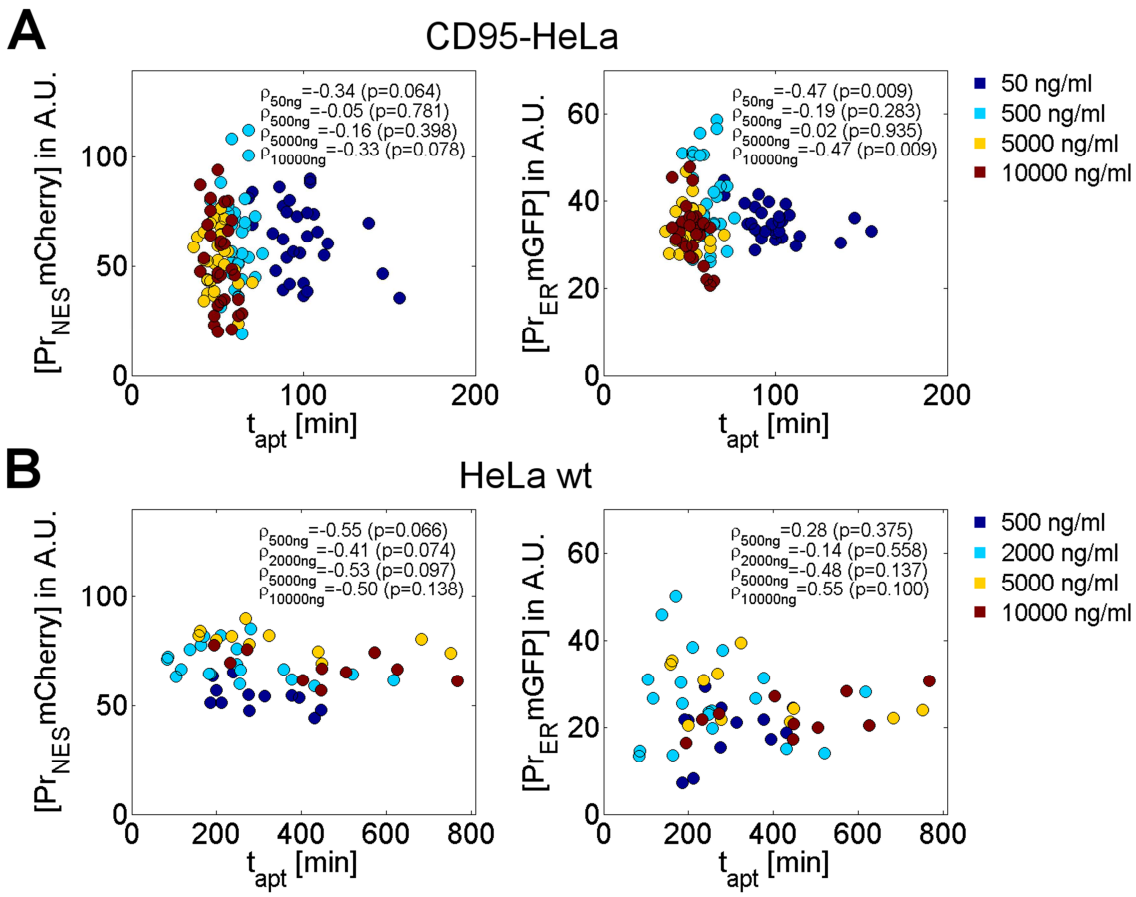

Figure S2. Total cleavage probe concentrations and apoptosis times. In CD95-HeLa (**A**) and wild-type HeLa cells (**B**), correlation coefficients were calculated for single cells at different ligand concentrations. The total amount of cleavage probes is not positively correlated with apoptosis time (left plots: cytosolic probe Pr_{NES}mCherry, right plots: ER-anchored probe Pr_{ER}mGFP). Correlation coefficients are listed on each graph for each concentration of ligand. Because active caspase-8 was not saturated by the cleavage probes, the assumption that the probe cleavage rates linearly depend on the concentrations of active caspase-8 species is valid.

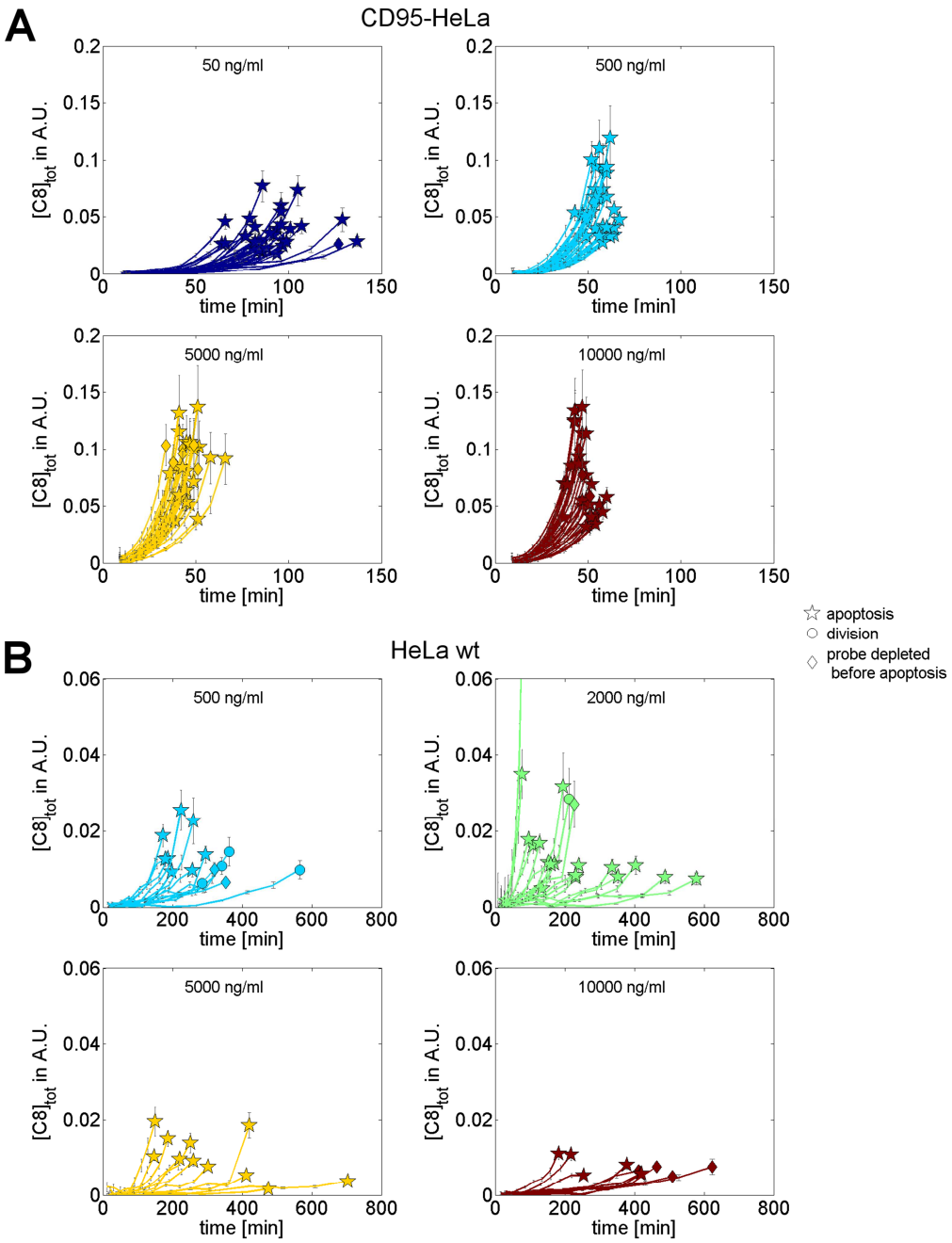

Figure S3. Single-cell caspase-8 trajectories for CD95-HeLa and wild-type HeLa cells. Trajectories for total caspase-8 (sum of p43 and p18 activities) in CD95-HeLa (**A**) and wild-type HeLa (**B**) cells at the indicated CD95L concentrations. In particular, single-cell trajectories of wild-type HeLa cells show decreased caspase-8 activity and delayed cell death at high ligand concentrations. The data presented in this figure are available in an Excel file (Caspase8SglCellData.xls) included in the additional Supplementary Materials. Error bars indicate propagated errors in caspase-8 activity calculations. The cell fates are indicated by symbols at the trajectory ends. In most cells apoptosis (stars) could be monitored. However, when cells started dividing (circles), the compartmentalization of the NES probes was lost. Therefore, we could not obtain data in mitotic cells undergoing apoptosis. In some cells, almost the total amount of cytoplasmic cleavage probes was cleaved before apoptosis (diamonds) and caspase-8 trajectories could not be further determined.

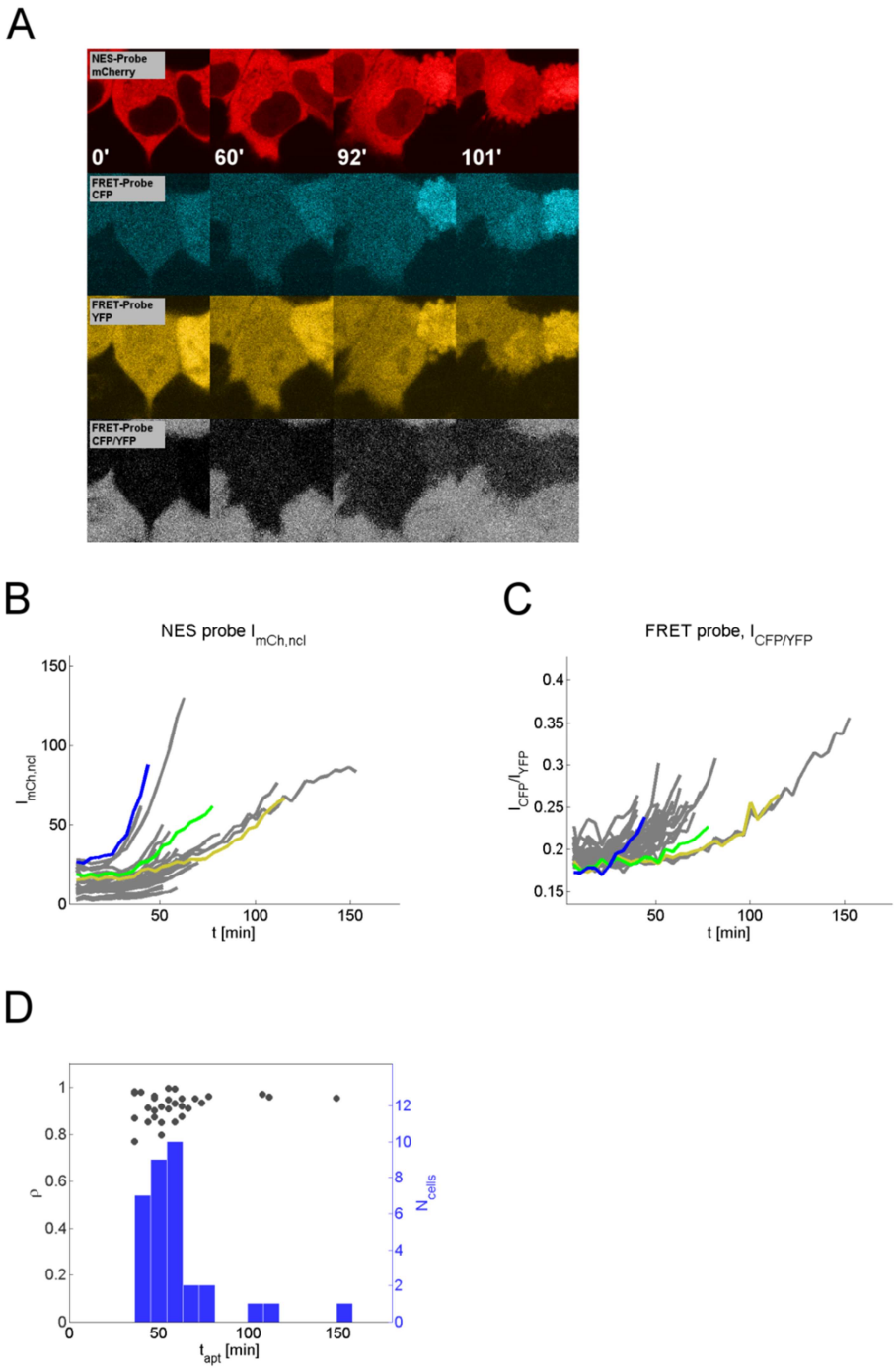

Figure S4. Single-cell trajectories for NES- and FRET-probe cleavage related to caspase-8 activity. (**A**) Live-cell confocal microscopic images for an exemplary cell that expresses NES- and FRET-cleavage probes. After cleavage of the nuclear export signal (NES) probe, the fluorescent protein mCherry enters the nucleus (upper row). Cleavage of the FRET-probe separates the two fluorescent proteins CFP and YFP. The loss of FRET is measured in the quotient of the intensities I_{CFP}/I_{YFP} (lower row). (**B**) Fluorescence intensity trajectories of all measured cells (n=33) were determined in ROIs within cross sections of the nuclei. (**C**) FRET signal trajectories of all measured cells. The quotients of the fluorescence intensities for CFP and YFP were measured in ROIs of cross sections of the entire cell. Representative cells are highlighted in green, blue, or yellow. (**D**) Correlation coefficients ρ between FRET- and NES-probe signal trajectories for each cell dependent on the time of cell death t_{apt}. The blue bars represent the numbers of cells that underwent cell death in a certain time interval. The lower correlation coefficients (indicated by gray dots) for cells with smaller t_{apt} can be explained by a lower number of data points at equal noise strength.

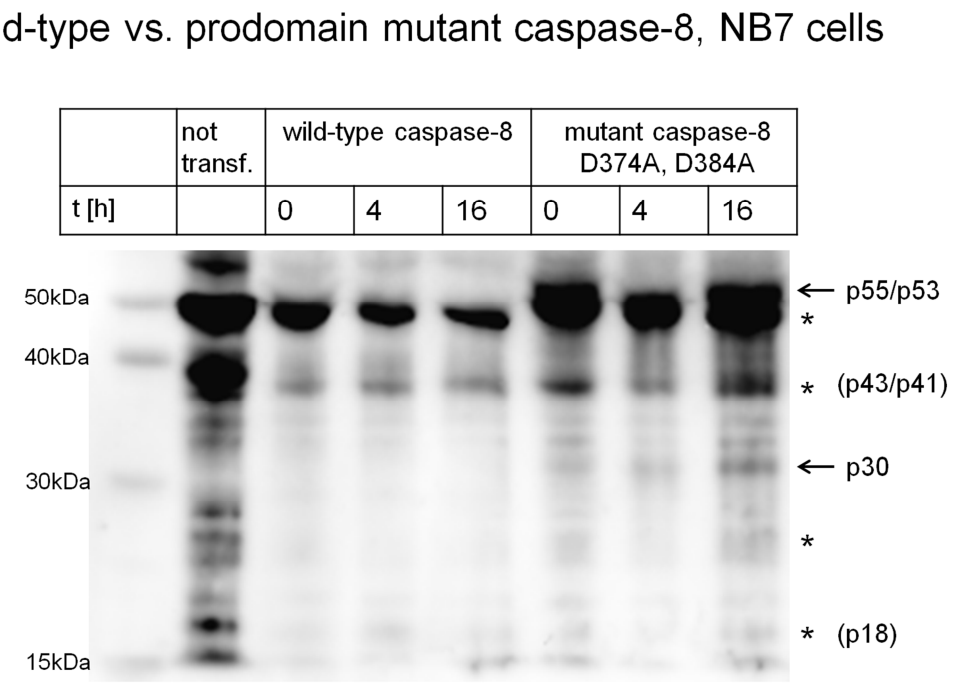

Figure S5. Western blot of wild-type and prodomain mutant caspase-8. Wild-type and prodomain mutant caspase-8 (D374A, D384A) were transiently expressed in the caspase-8-deficient, CD95-deficient, TRAIL receptor-expressing NB7 cell line (human neuroblastoma). Cells expressing wild-type or mutant caspase-8 were stimulated for the indicated times with 200 ng/ml TRAIL. In the prodomain mutant form, unprocessed p55/p53 and p30 can be detected. Nonspecific bands (*) were present in all samples (first lane: marker bands, second lane: lysate from non-transfected cells). The band of p55/53 is flanked by a nonspecific band, and the bands of p43/41 and p18 are covered by nonspecific bands. Peptides were detected with C-15 antibody.

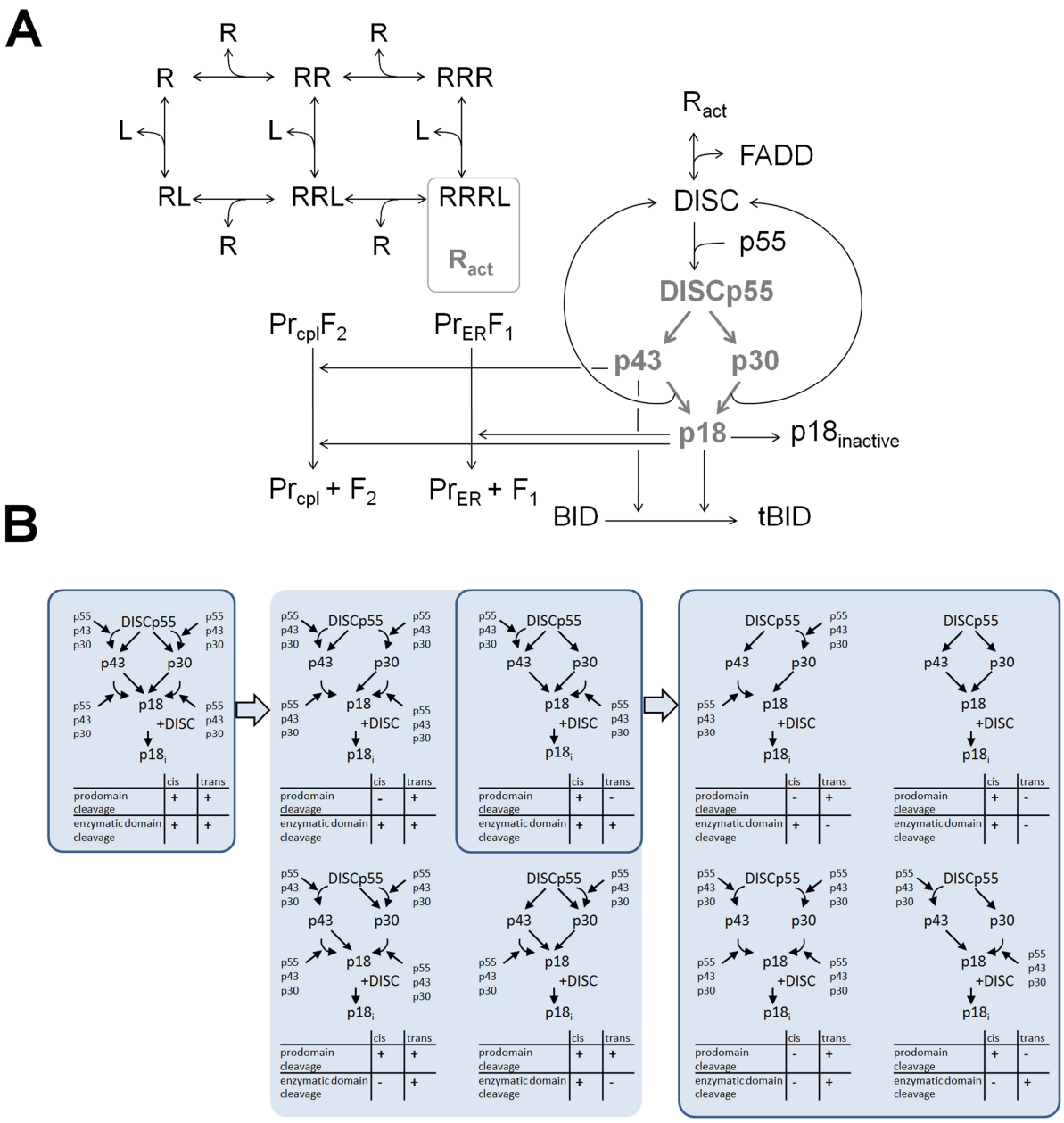

Figure S6. Model graphs for oligomerization-driven receptor activation and caspase-8 activation. (**A**) Cell death receptors R can oligomerize to dimers and trimers. Cell death ligands L can bind to monomeric, dimeric, or trimeric receptors. Only ligand-bound receptor trimers RRRL are active receptors (R_{act}) that serve as a platform for DISC formation and caspase-8 activation. A steady-state solution for the receptor oligomerization model was combined with a model of caspase-8 activation. Here, the full topology of the 'cis/cis' variant is represented, in which cleavages of the prodomain and enzymatic domain sites are described as unimolecular reactions. (**B**) Hypotheses that prodomain or enzymatic domain sites are cleaved in cis or trans mechanisms lead to nine alternative model topologies. The full topology, in which both sites are cleaved in cis *and* trans can be simplified to four minimal topologies, in which only two cleavage modes are possible. The variants surrounded by boxes were fitted to experimental data.

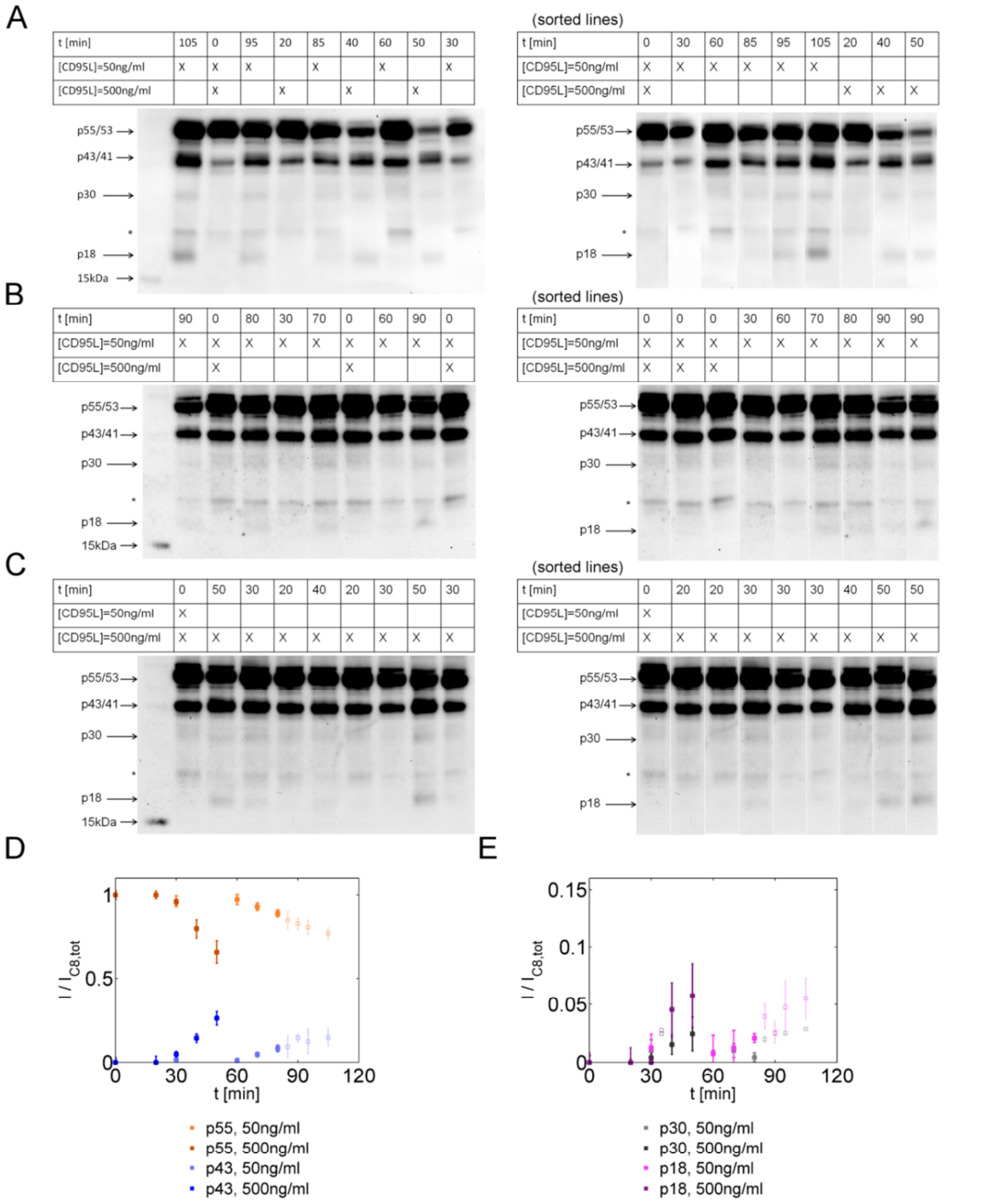

Figure S7. Caspase-8 Western blot time series were used for model fitting of population observables. It was assumed that the employed antibody binds equally well to procaspsae-8 and its products. (**A**-**C**) Exemplary Western blots from experiments in CD95-HeLa cells exposed to the indicated concentrations of CD95L for the indicated times. For each data point included in model fitting three replicates were measured. The order of samples was shuffled to avoid biases from gel and blotting inhomogeneities (61). Intensities of every band were background corrected and normalized to the sum of all caspase-8 bands (p55/53, p43/41, p30, and p18). Western blots are shown with original orders of lines (left plots) and sorted (cut and reassembled) according to time points and experiments (right plots). An unspecific band is marked by a star. (**D**) Background-corrected and normalized intensities for p55 and p43 of at least three replicates were used for model fitting at times before cells started to undergo apoptosis (until 80 minutes for [CD95L] = 50 ng/ml and until 50 minutes for [CD95L] = 500 ng/ml). Time points included for model fitting are displayed as solid symbols and not included time points as empty symbols (error bars: standard error of the mean). (**E**) Background-corrected and normalized intensities for p30 and p18 as in (D).

A

t [min]	105	0	95	20	85	40	60	50	30
[CD95L]=50ng/ml	X		X		X		X		X
[CD95L]=500ng/ml		X		X		X		X	

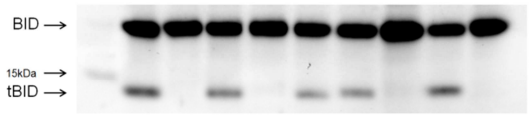

B

t [min]	80	0	70	30	0	90	70	80	0
[CD95L]=50ng/ml	X		X	X	X	X	X	X	
[CD95L]=500ng/ml		X							X

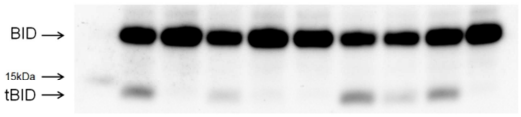

C

t [min]	0	50	30	20	40	20	30	50	30
[CD95L]=50ng/ml									
[CD95L]=500ng/ml	X	X	X	X	X	X	X	X	X

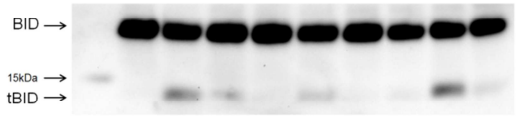

D

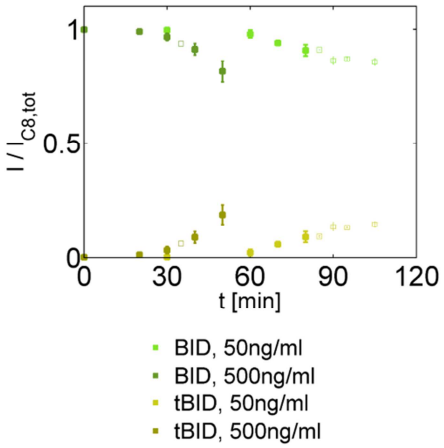

Figure S8. BID and tBID Western blot time series served for model fitting of population observables. (**A**-**C**) As for caspase-8, for each time point included in model fitting three replicates were measured in CD95-HeLa cells at 50 ng/ml and 500 ng/ml. Intensities of every band were background corrected and normalized to the sum of BID and tBID. (**D**) As described in figure S7 for caspase-8, background-subtracted and normalized intensities of at least three replicates were used for model fitting before the first cells underwent apoptosis (solid symbols – time points included for model fitting, empty squares – not included data points).

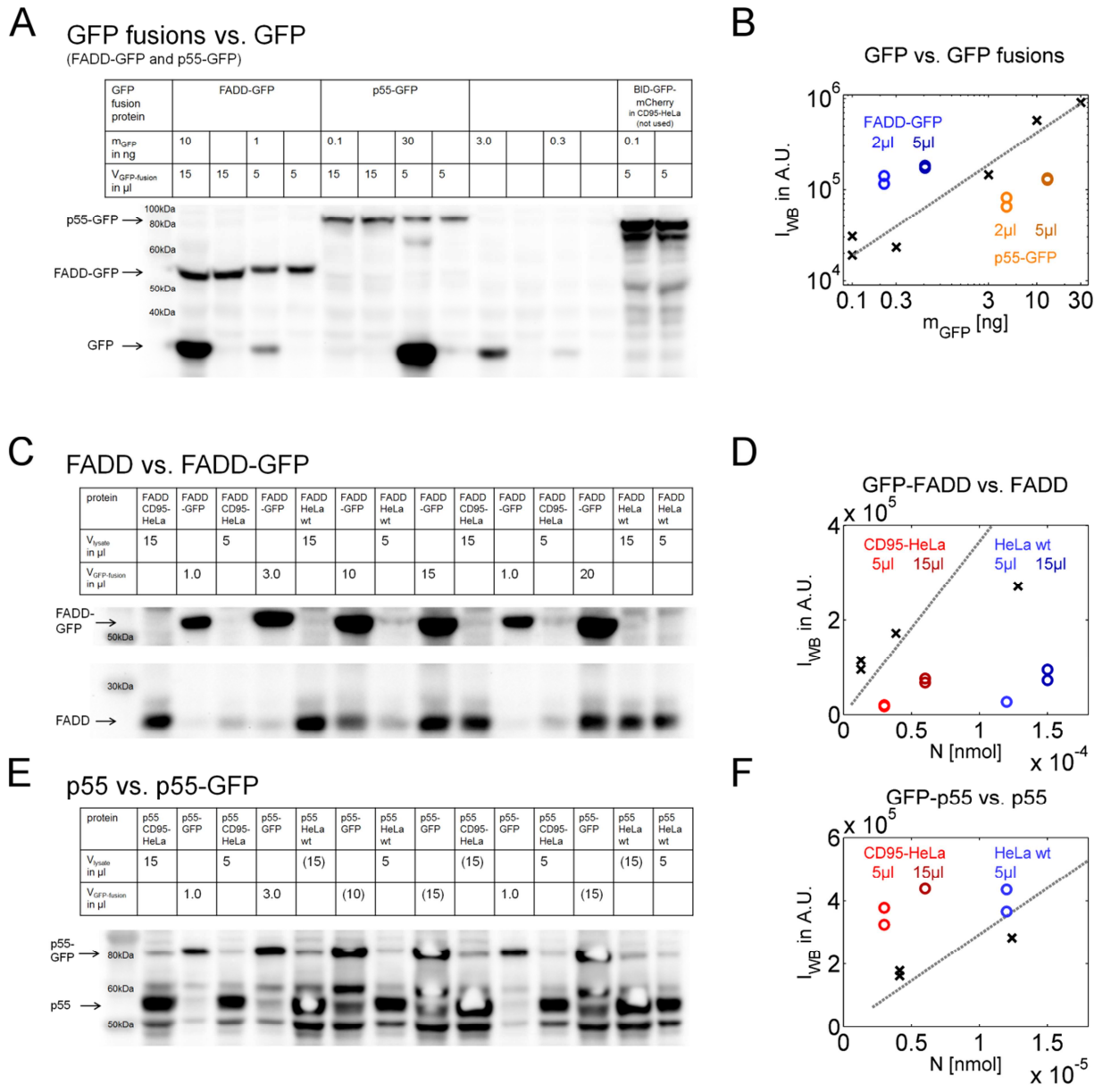

Figure S9. Estimation of average FADD and p55 amounts by calibrated Western blot. (**A**) Blotting FADD-GFP and p55-GFP together with doses of recombinant GFP served to estimate concentrations of FADD and p55 fusions. (**B**) Calibration curve of GFP (x) and amount of FADD-GFP or p55-GFP in two different volumes of lysate. (**C**, **D**) FADD amounts were estimated by simultaneously blotting FADD-GFP lysate doses were blotted together with 5 µl or 15 µl of lysates from probe-expressing cells. In panel (C) a part of the blot between 30 kD and 50 kD was cut out. (**E**, **F**) p55 amounts were estimated by simultaneously blotting p55-GFP lysate doses with lysates from probe-expressing cells. Intensities were background corrected. Values in brackets indicate oversaturated bands (bands with white spots) that were excluded from evaluations. Estimates had the same order of magnitude as in Fricker *et al*. (25): N_{FADD}≈200.000/cell in our study compared to 130.000/cell in Fricker *et al*., and N_{p55}≈320.000 in our study compared to 250.000/cell in Fricker *et al*.

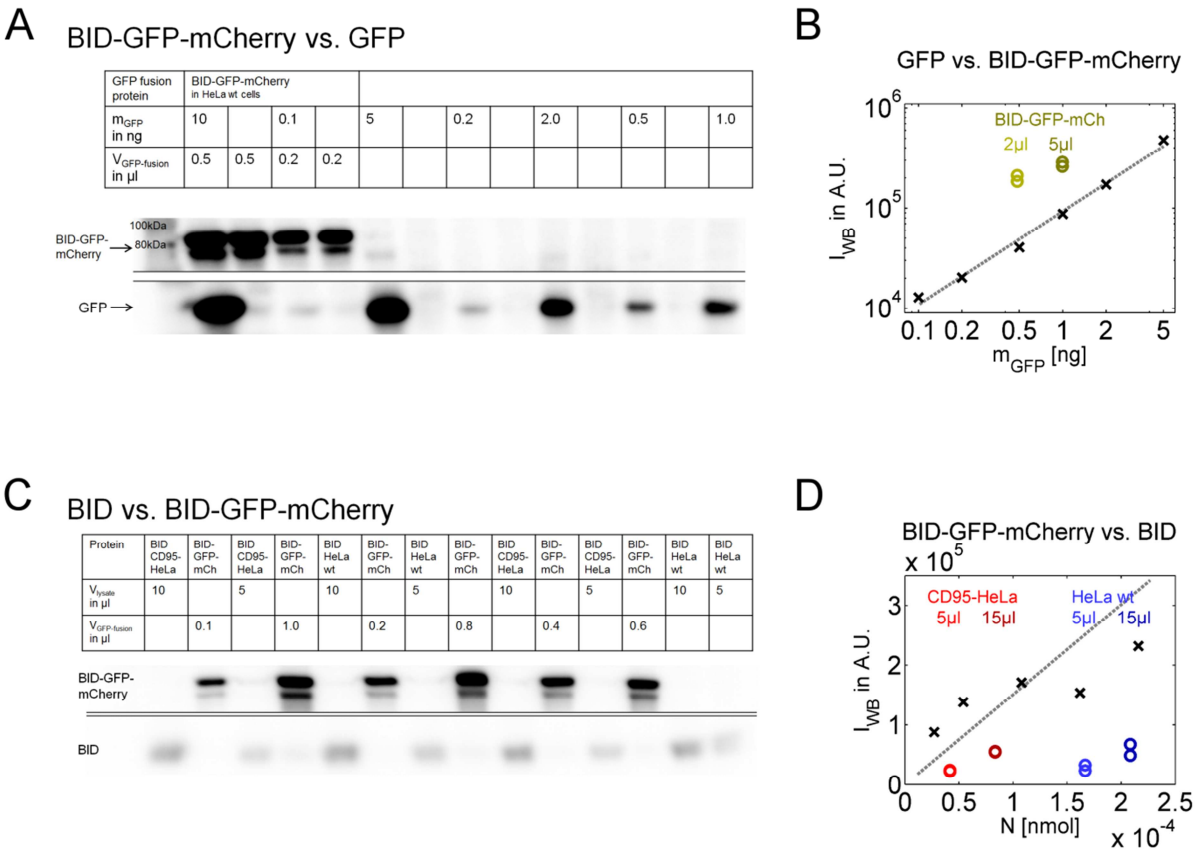

Figure S10. Estimation of average BID amounts by calibrated Western blot. (**A**, **B**) BID-GFP-mCherry amounts were calibrated by blotting together with doses of recombinant GFP. (**C**, **D**) BID numbers in probe-expressing CD95-HeLa and wild-type HeLa cells were estimated by blotting together with BID-GFP lysates. Black lines indicate that sections of intermediate range in size were cut out. Data analysis as described in figure S9.

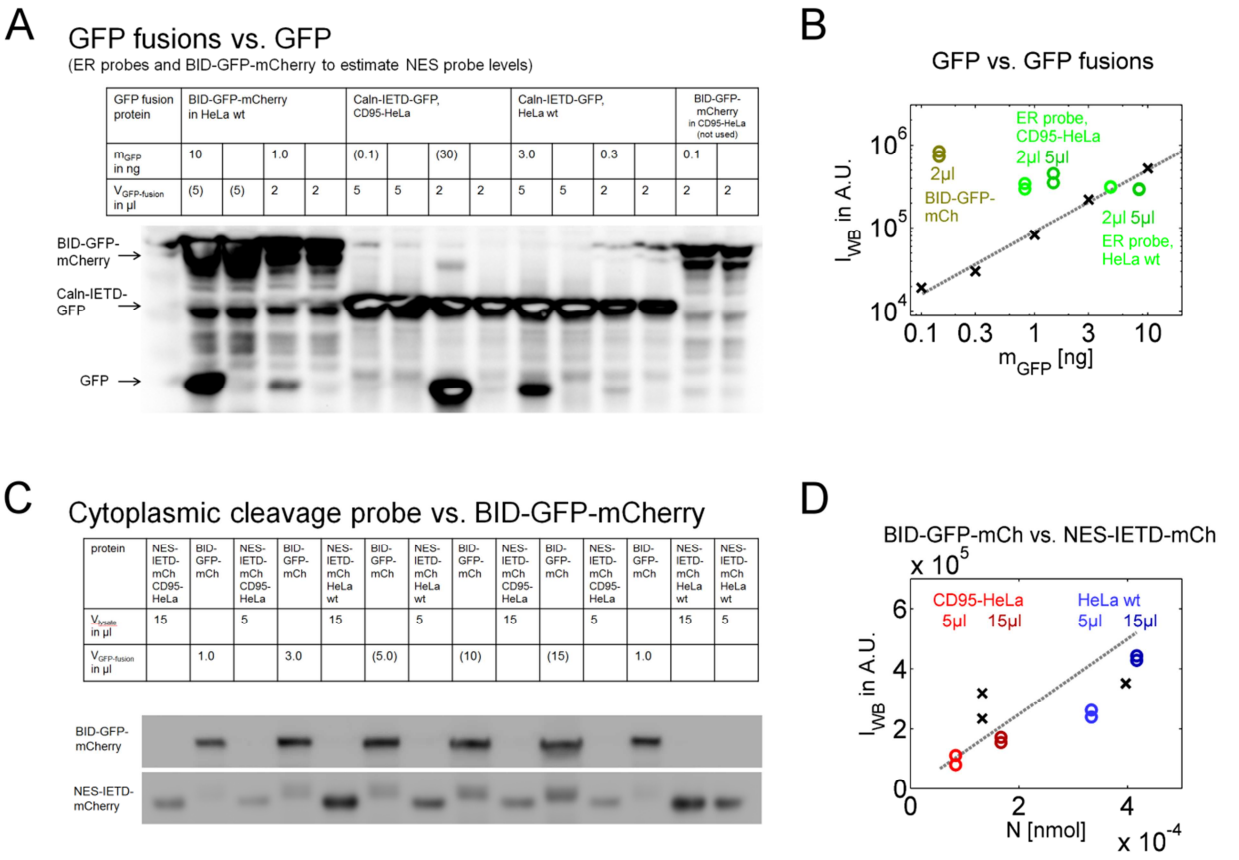

GFP fusion protein	BID-GFP-mCherry in HeLa wt				Caln-IETD-GFP, CD95-HeLa				Caln-IETD-GFP, HeLa wt				BID-GFP-mCherry in CD95-HeLa (not used)	
m_{GFP} in ng	10		1.0		(0.1)		(30)		3.0		0.3		0.1	
$V_{GFP\text{-}fusion}$ in µl	(5)	(5)	2	2	5	5	2	2	5	5	2	2	2	2

protein	NES-IETD-mCh CD95-HeLa	BID-GFP-mCh	NES-IETD-mCh CD95-HeLa	BID-GFP-mCh	NES-IETD-mCh HeLa wt	BID-GFP-mCh	NES-IETD-mCh HeLa wt	BID-GFP-mCh	NES-IETD-mCh CD95-HeLa	BID-GFP-mCh	NES-IETD-mCh CD95-HeLa	BID-GFP-mCh	NES-IETD-mCh HeLa wt	NES-IETD-mCh HeLa wt
V_{lysate} in µl	15		5		15		5		15		5		15	5
$V_{GFP\text{-}fusion}$ in µl		1.0		3.0		(5.0)		(10)		(15)		1.0		

Figure S11. Estimation of average cleavage probe amounts by calibrated Western blot. (**A**, **B**) Amounts of ER-anchored probes (Calnexin-GIETDS-GFP) were directly estimated by blotting lysates of probe-expressing cells together with recombinant GFP (B). BID-GFP-mCherry, expressed in wild-type HeLa cells, was calibrated with recombinant GFP to estimate cytosolic probe (NES-GIETDS-mCherry) amounts (abbreviations: caln – calnexin, mCh – mCherry). Values in brackets indicate oversaturated bands that were excluded from evaluations. Bands for ER probes were evaluated despite signs of oversaturation because it was sufficient to estimate lower boundaries of protein numbers ($N_{ER\ probes} \geq 8 \cdot 10^6$/cell). (**C**, **D**) To estimate cytosolic probe amounts, probe-expressing cell lysates were blotted together with BID-GFP-mCherry lysate. In panel (C), a section of intermediate range in size was spliced out. Data analysis as described in figure S9.

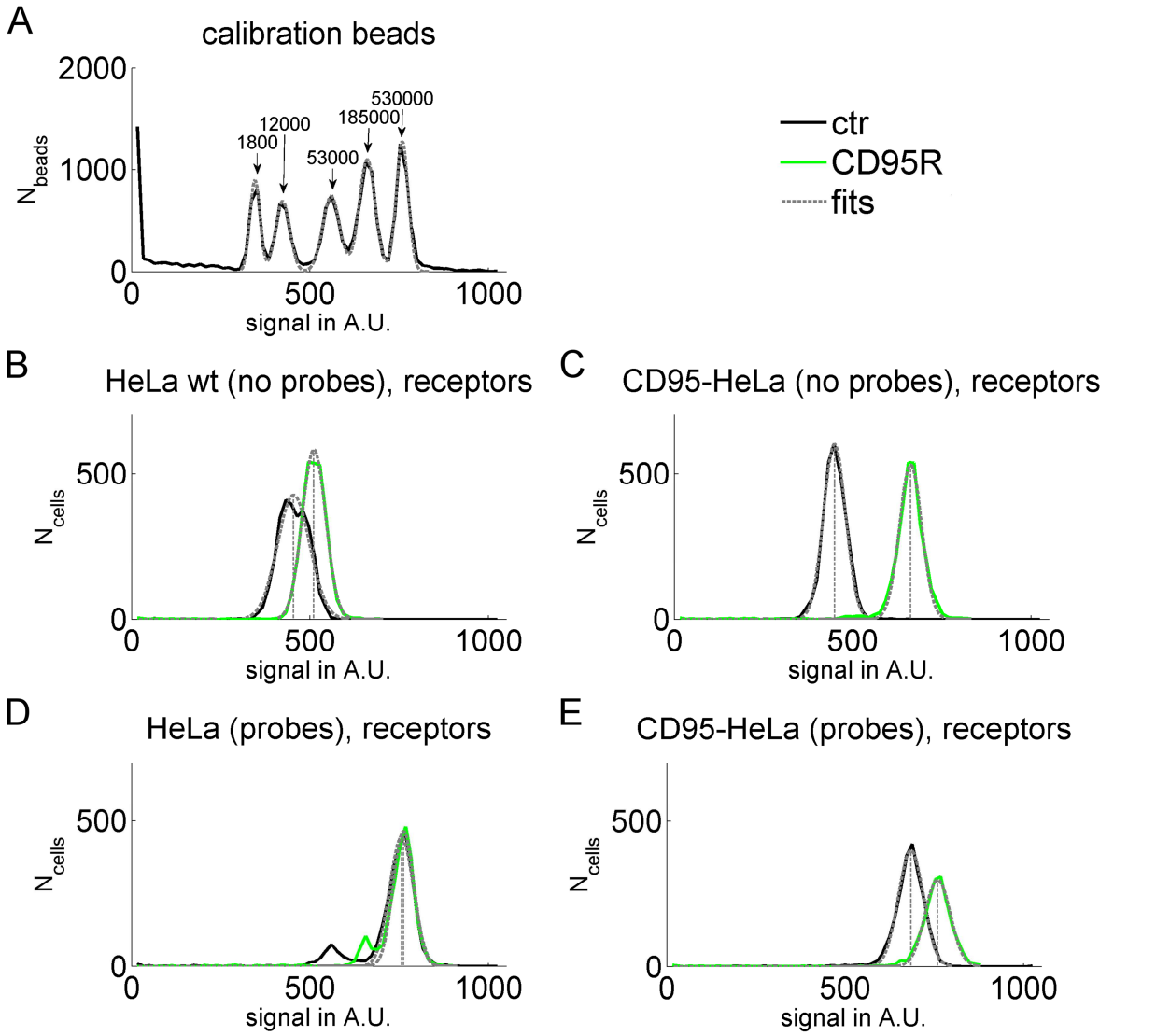

Figure S12. Flow cytometry of cells immunostained for CD95. (**A**) To estimate average numbers of membrane-bound receptors, beads with five different numbers of epitopes for fluorescent-labeled secondary antibodies were used to calibrate the FACS signal. In wild-type HeLa (**B**) or CD95-HeLa (**C**) and probe-expressing wild-type HeLa (**D**) or CD95-HeLa (**E**) cells, receptor numbers were estimated by fitting normal distribution functions ('fits') and subtracting background signals of control measurements ('ctr').

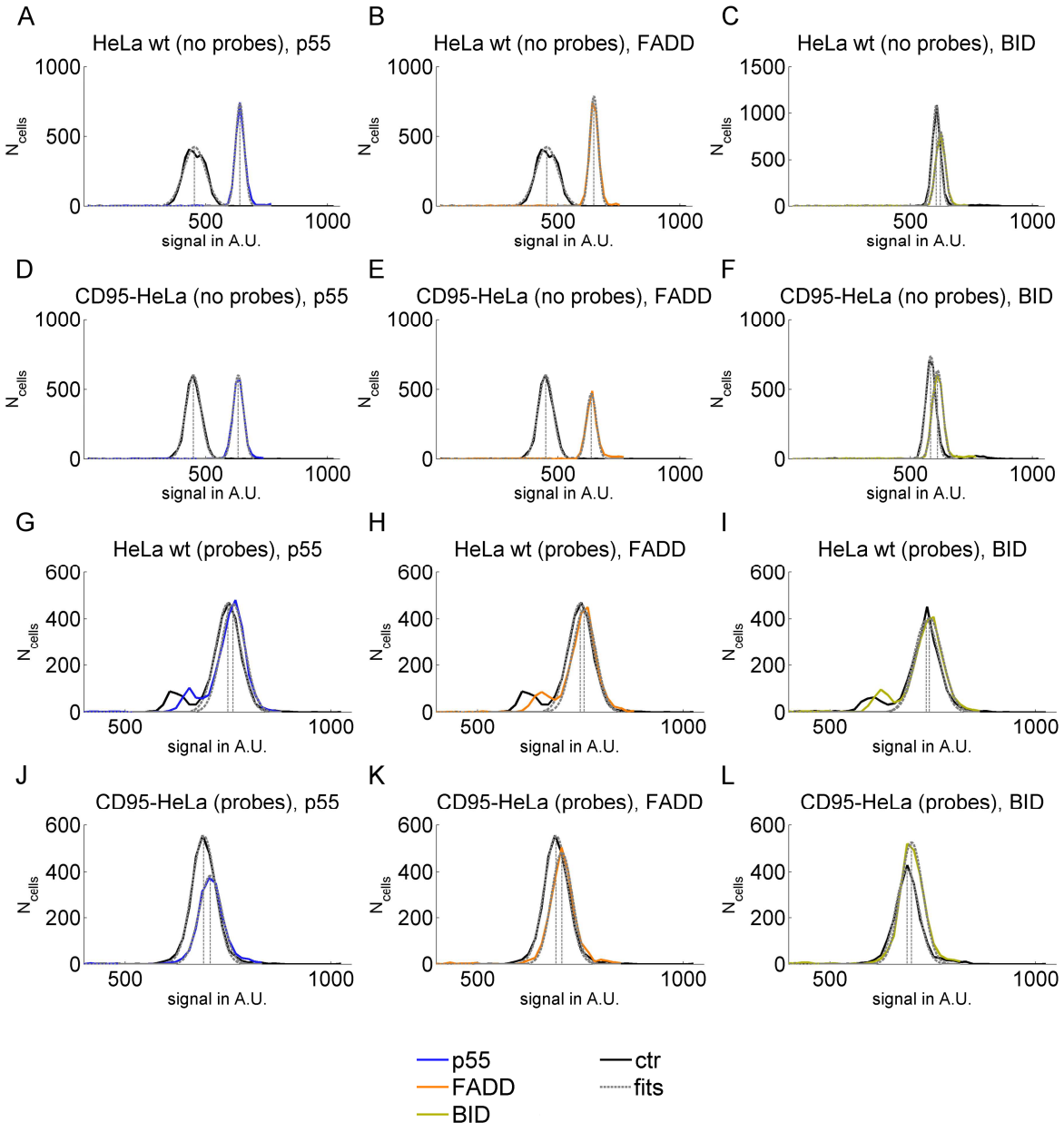

Figure S13. Flow cytometry of cells immunostained for p55, FADD, and BID. Nontransfected wild-type HeLa (**A**-**C**) and CD95-HeLa (**D**-**F**), as well as probe-expressing wild-type HeLa (**G**-**I**) and CD95-HeLa cells (**J**-**L**) were stained for the indicated proteins. Normal distribution functions were fitted to cells stained with primary antibodies (fits) and control (ctr) measurements.

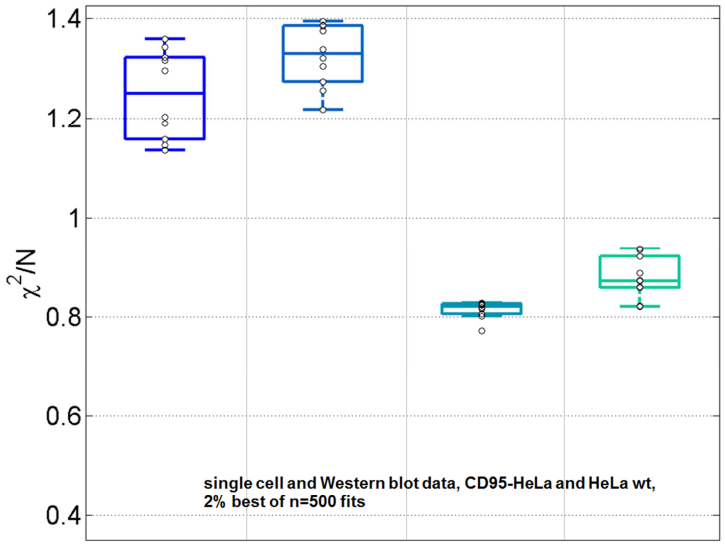

prodomain cleavage	cis $k_{prodomain,p55} \neq k_{prodomain,p43}$	cis $k_{prodomain,p55} = k_{prodomain,p43}$	cis $k_{prodomain,p55} \neq k_{prodomain,p43}$	cis $k_{prodomain,p55} = k_{prodomain,p43}$
enzymatic domain cleavage	cis	cis	trans	trans

Figure S14. Fit qualities of extended cis/cis and cis/trans model variants. Cis cleavage of p43 to p18 could be faster than cis cleavage of p55 to p30, or both reactions could have equal speed because the same site is cleaved. Therefore, cis cleavage of the prodomain site can be described with either different or equal kinetic constants for cleavage reactions from p55 to p30 ($k_{prodomain,p55}$) and from p43 ($k_{prodomain,p43}$) to p18. We tested this hypothesis in the rejected 'cis/cis' topology and the 'cis/trans' topology, which was the best-fitting smallest model variant. As indicated by χ^2/N values for the best fits, models with unequal constants do not improve fit quality substantially compared to models with equal parameters.

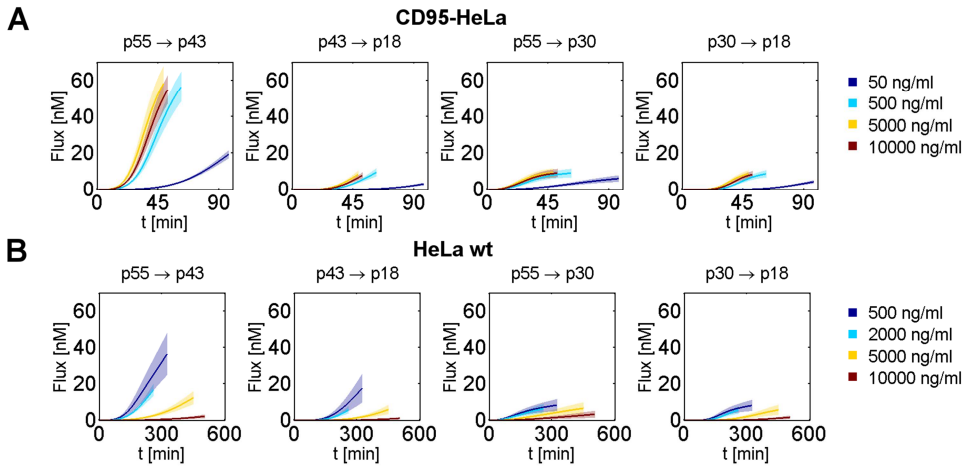

Figure S15. Reaction fluxes for the cis+trans/cis+trans topology in separate cleavage reactions. (**A**) Starting from the median estimated initial concentrations, given by the best 1% of n=1000 model fits to the full data set (single-cell and population data), reaction fluxes were integrated until the median cell death time at different ligand concentrations to monitor the contributions of cleavage reactions. Solid lines represent mean trajectories and shaded areas 1σ confidence intervals. At every ligand concentration, the largest amount of initial p55 is processed in the reaction from p55 to p43, whereas only minor amounts are processed from p43 to p18 and in the alternative route from p55 through p30 to p18. Changing ligand concentrations has the strongest effect on the reaction from p55 to p43, which can be explained by weaker positive feedback from trans cleavage by p43. (**B**) Integrated fluxes for cleavage reactions in wild-type HeLa cells, analogous to (A). As in CD95-HeLa cells, the reaction from p55 to p43 has the largest fluxes, whereas the relative difference to the other cleavage reactions is smaller. Compared to reactions in CD95-HeLa cells, larger amounts of p18 are generated relative to p43 before undergoing apoptosis.

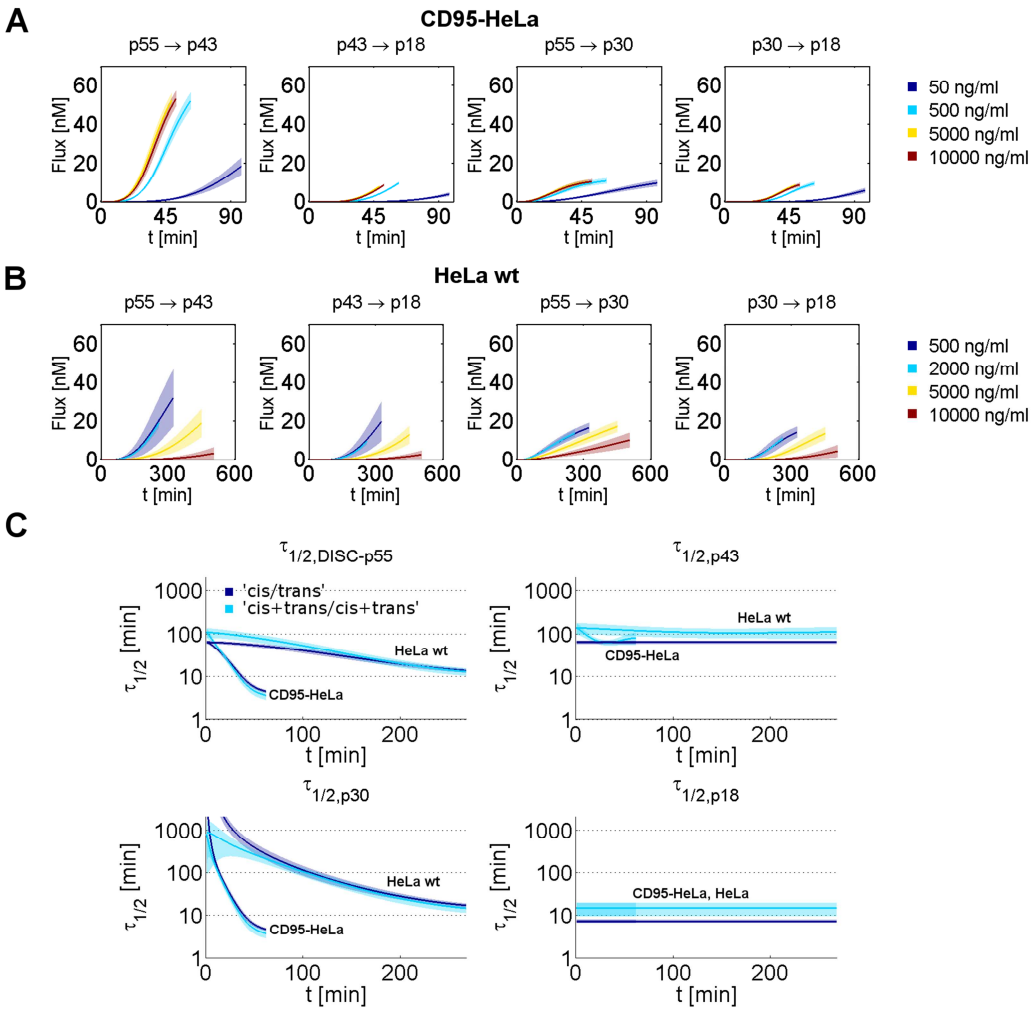

Figure S16. Reaction fluxes and half-lives of caspase-8 intermediates for the cis/trans topology. Integrated reaction fluxes are plotted for procaspase-8 cleavage for CD95-HeLa (**A**) and for wild-type HeLa cells (**B**). (**C**) Comparison between model estimates of protein half-lives between the 'cis/trans' and the 'cis+trans/cis+trans' model variants for CD95-HeLa and wild-type HeLa cells. Solid lines represent mean trajectories and shaded areas represent standard deviations from the best 1% of 1000 fits to the complete set of single-cell and population data.

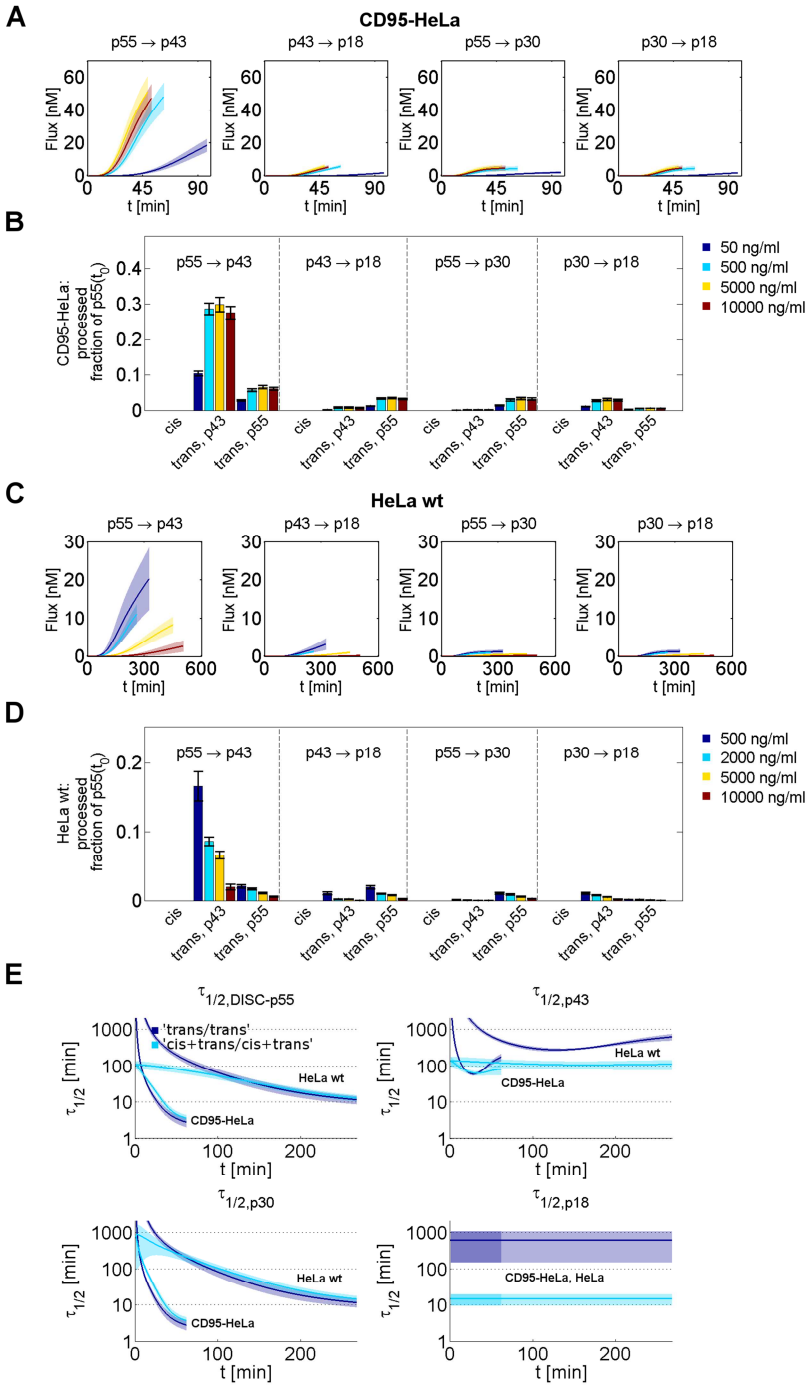

Figure S17. Reaction fluxes and half-lives of caspase-8 intermediates for the trans/trans topology. Integrated reaction fluxes are plotted for procaspase-8 cleavage for CD95-HeLa (**A**) and for wild-type HeLa (**C**) cells. Panels (**B**) and (**D**) show fractions of the initial p55 concentration that are processed within the different cleavage reactions. Whereas p43 has a stronger trans cleavage activity in the enzymatic domain cleavage reactions (p55 to p43, p30 to p18); p55 has stronger trans cleavage activity for prodomain cleavage reactions (p55 to p30, p43 to p18). (**E**) Comparison between model estimates of protein half-life times between the 'trans/trans' and the 'cis+trans/cis+trans' model variants for CD95-HeLa and wild-type HeLa cells. Solid lines represent mean trajectories and shaded areas represent standard deviations from the best 1% of 1000 fits to the complete set of single-cell and population data,.

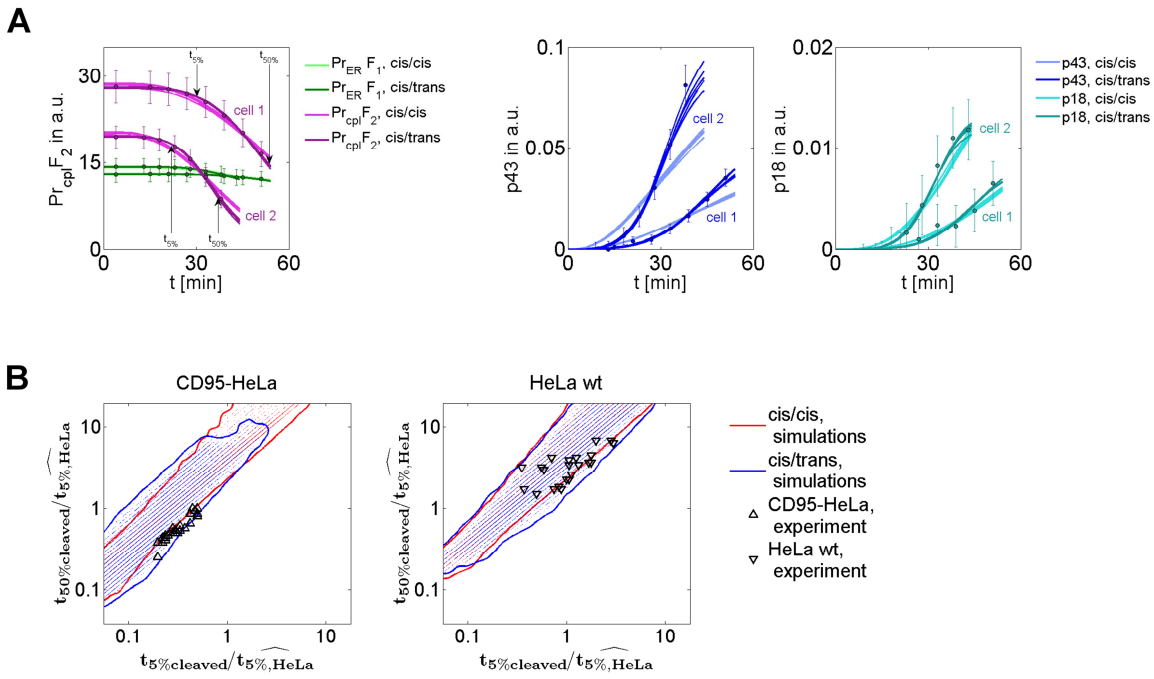

Figure S18. Monte Carlo modeling supports discrimination between cis/cis and cis/trans topologies. (**A**) Model fits of 'cis/cis' and 'cis/trans' versions to data of two exemplary cells as in Fig. 5E. In the left plot, times until 5% or 50% cytosolic probe cleavage, $t_{5\%}$ and $t_{50\%}$, are indicated. (**B**) Combinations of normalized $t_{5\%}$ and $t_{50\%}$ experimental values for CD95-HeLa cells fit into the space of simulated 'cis/trans' trajectories bounded by blue lines, but not into the space of simulated 'cis/cis' trajectories bounded by red lines. However, for wild-type HeLa cells a direct discrimination by the $t_{5\%}$ and $t_{50\%}$ measures is not possible as most of the experimental values are compatible with simulated values from the 'cis/trans' and the 'cis/cis' versions. Time points extracted from simulated trajectories are shown as dots. Solid lines mark borders of dot densities that include 99% of simulated values. To obtain a collective timescale, time points were normalized by the mean of $t_{5\%}$ values for wild-type HeLa cells ( ).

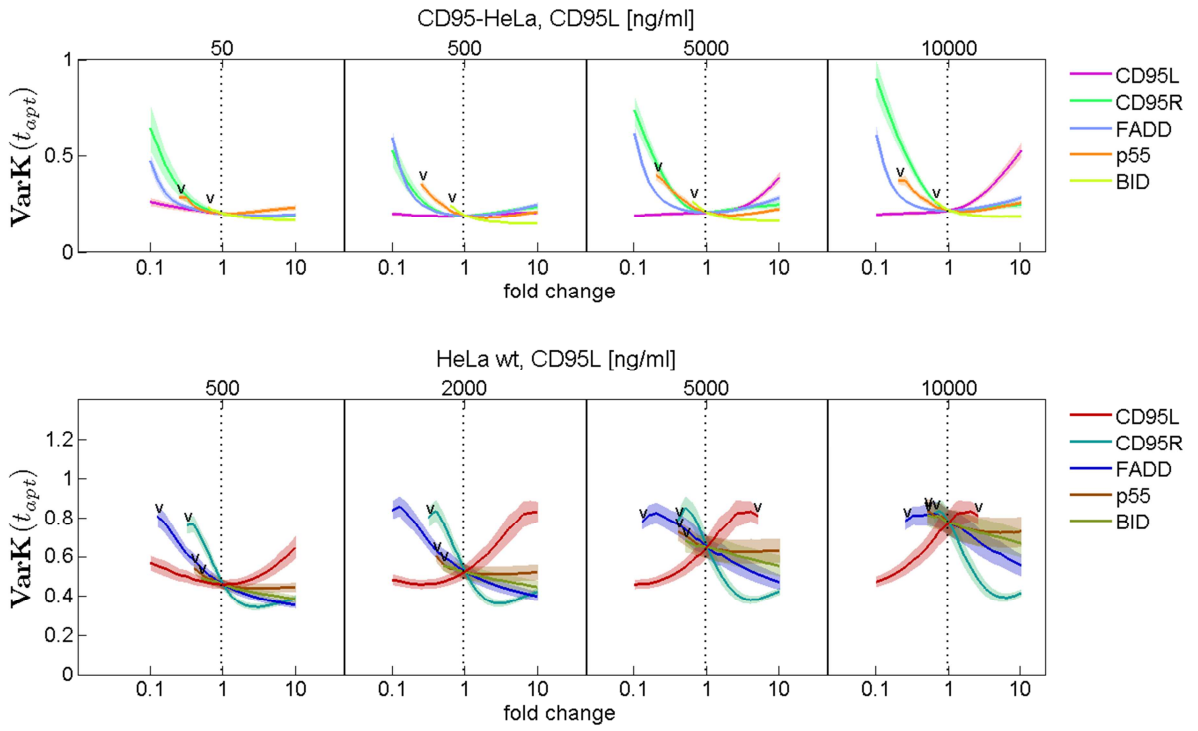

Figure S19. Predicted coefficients of variation of apoptosis times at different CD95 ligand concentrations. The effects of fold changes between one tenth and ten times of the initial protein concentrations were simulated. Simulations for [CD95L] = 500 ng/ml correspond to Fig. 7B and 7C. Shaded areas show standard deviations from the best 1% of n = 1000 fits.

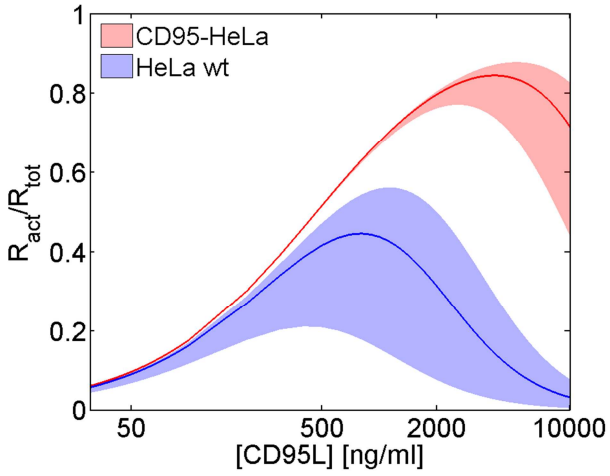

Figure S20. Variability of active receptor fractions for CD95-HeLa, and wild-type HeLa cells. Mean fractions (lines) and areas for 1σ confidence intervals for single cells with different receptor concentrations and saturation thresholds (shaded areas) for the best 'cis/trans' model fit.

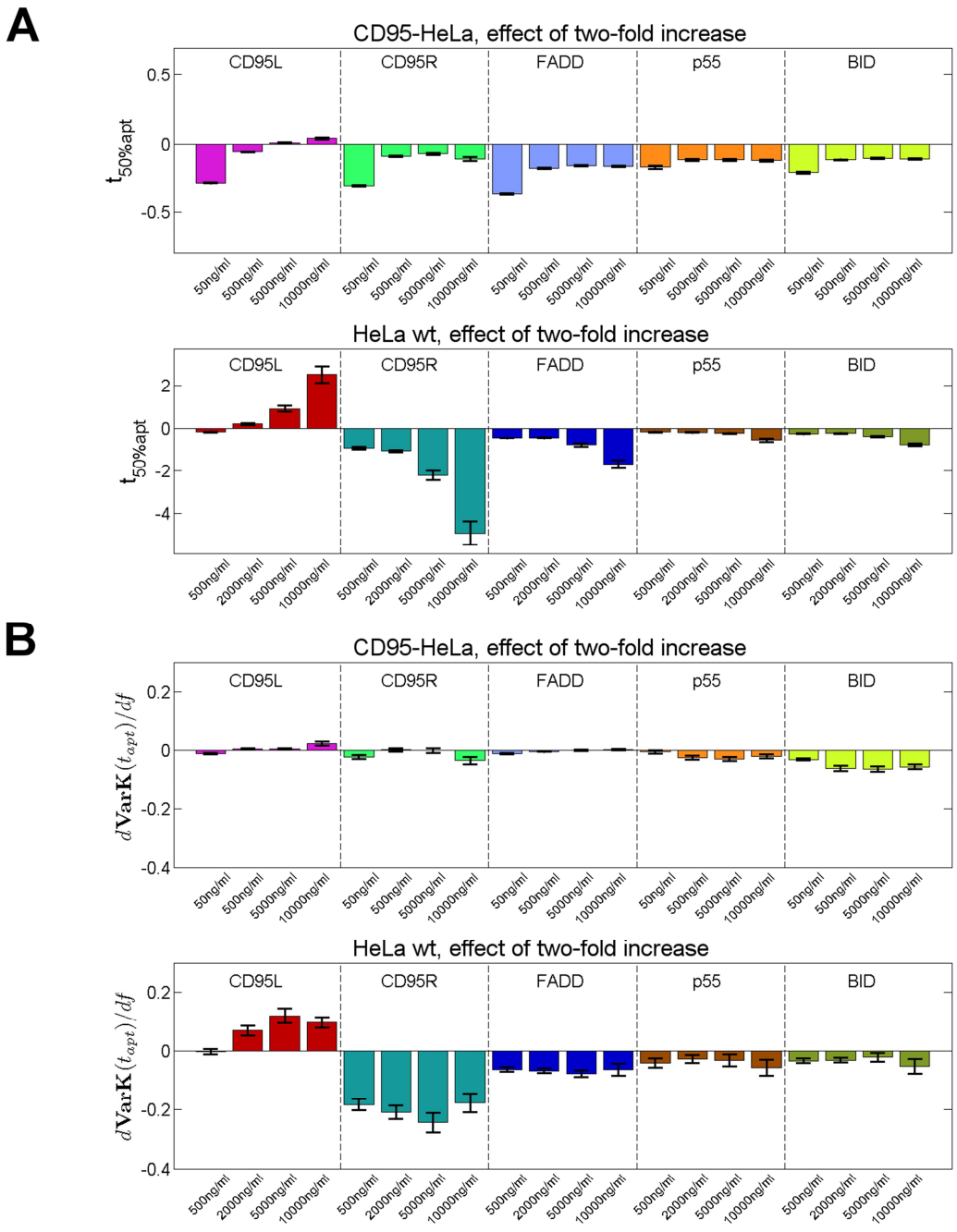

Figure S21. Model predictions of the effects of twofold increases in initial protein concentrations. For estimations from each of the best 1% of n = 1000 fits ('cis/trans' variant fitted to the whole set of experimental data), One hundred sets of initial protein concentrations were randomly sampled from multivariate joint distributions of estimated initial concentrations for CD95R, FADD, p55, and BID, as well as tBID thresholds. (**A**) Effects of two-fold increases in initial protein concentrations in CD95-HeLa (upper row) or wild-type HeLa cells (lower row) on median cell death times at the ligand concentrations that were used in single-cell experiments. Bars represent effects of two-fold changes around the origin. I(**B**) Effects of two-fold increases in initial protein concentrations on coefficients of variation of cell death times. Error bars in panels (A) and (B) show standard deviations from the best 1% of n = 1000 fits.

Table S1. Reactions of the complete model cis+trans/cis+trans and smaller variants.

model reactions
'cis/cis': (1)-(4),(8),(12),(16),(20)-(25)
'cis/trans': (1)-(4),(9)-(11),(13)-(16),(20)-(25)
'cis+trans/cis+trans': (1)-(25)

$$CD95_{active} + FADD \xrightarrow{k_{on,FADD}} DISC \quad (1)$$

$$DISC \xrightarrow{k_{off,FADD}} CD95_{active} + FADD \quad (2)$$

$$DISC + p55 \xrightarrow{k_{on,p55}} DISC\_p55 \quad (3)$$

$$DISC\_p55 \xrightarrow{k_{cl,prodomain,cis}} p30 \quad (4)$$

$$DISC\_p55 + DISC\_p55 \xrightarrow{k_{cl,prodomain,trans,p55}} p30 + DISC\_p55 \quad (5)$$

$$DISC\_p55 + p30 \xrightarrow{k_{cl,prodomain,trans,p55}} p30 + p30 \quad (6)$$

$$DISC\_p55 + p43 \xrightarrow{k_{cl,prodomain,trans,p43}} p30 + p43 \quad (7)$$

$$DISC\_p55 \xrightarrow{k_{cl,enz.domain,cis}} p43 \quad (8)$$

$$DISC\_p55 + DISC\_p55 \xrightarrow{k_{cl,enz.domain,trans,p55}} p43 + DISC\_p55 \quad (9)$$

$$DISC\_p55 + p30 \xrightarrow{k_{cl,enz.domain,trans,p55}} p43 + p30 \quad (10)$$

$$DISC\_p55 + p43 \xrightarrow{k_{cl,enz.domain,trans,p43}} p43 + p43 \quad (11)$$

$$p30 \xrightarrow{k_{cl,enz.domain,cis}} p18 + DISC \quad (12)$$

$$p30 + DISC\_p55 \xrightarrow{k_{cl,enz.domain,trans,p55}} p18 + DISC + DISC\_p55 \quad (13)$$

$$p30 + p30 \xrightarrow{k_{cl,enz.domain,trans,p55}} p18 + DISC + p30 \quad (14)$$

$$p30 + p43 \xrightarrow{k_{cl,enz.domain,trans,p43}} p18 + DISC + p43 \quad (15)$$

$$p43 \xrightarrow{k_{cl,prodomain,cis}} p18 + DISC \quad (16)$$

$$p43 + DISC\_p55 \xrightarrow{k_{cl,prodomain,trans,p55}} p18 + DISC + DISC\_p55 \quad (17)$$

$$p43 + p30 \xrightarrow{k_{cl,prodomain,trans,p55}} p18 + DISC + p30 \quad (18)$$

$$p43 + p43 \xrightarrow{k_{cl,prodomain,trans,p43}} p18 + DISC + p43 \quad (19)$$

$$p18 \xrightarrow{k_{p18.inactive}} p18_{inactive} \quad (20)$$

$$BID + p18 \xrightarrow{k_{cl,BID}} tBID + p18 \quad (21)$$

$$BID + p43 \xrightarrow{k_{cl,BID}} tBID + p43 \quad (22)$$

$$Pr_{ER}mGFP + p18 \xrightarrow{k_{cl,probe}} Pr_{ER} + mGFP + p18 \quad (23)$$

$$Pr_{NES}mCherry + p18 \xrightarrow{k_{cl,probe}} Pr_{NES} + mCherry + p18 \quad (24)$$

$$Pr_{NES}mCherry + p43 \xrightarrow{k_{cl,probe}} Pr_{NES} + mCherry + p43 \quad (25)$$

Table S2. Reaction rates in the complete cis+trans/cis+trans model and smaller variants.

reaction rates	
$v_1 = k_{on,FADD}[CD95_{active}][FADD]$	$v_{11} = k_{cl,enz.domain,trans,p55}[p30]$ $([DISC\_p55] + [p30])$
$v_2 = k_{off,FADD}[DISC]$	$v_{12} = k_{cl,enz.domain,trans,p43}[p30][p43]$
$v_3 = k_{on,p55}[DISC][p55]$	$v_{13} = k_{cl,prodomain,cis}[p43]$
$v_4 = k_{cl,prodomain,cis}[DISC\_p55]$	$v_{14} = k_{cl,promdomain,trans,p55}[p43]$ $([DISC\_p55] + [p30])$
$v_5 = k_{cl,prodomain,trans,p55}[DISC\_p55]$ $([DISC\_p55] + [p30])$	$v_{15} = k_{cl,prodomain,trans,p43}[p43]^2$
$v_6 = k_{cl,prodomain,trans,p43}[DISC\_p55][p43]$	$v_{16} = k_{p18,inactive}[p18]$
$v_7 = k_{cl,enz.domain,cis}[DISC\_p55]$	$v_{17} = k_{cl,BID}[BID]([p43] + [p18])$
$v_8 = k_{cl,enz.domain,trans,p55}[DISC\_p55]$ $([DISC\_p55] + [p30])$	$v_{18} = k_{cl,probe}[Pr_{ER}mGFP][p18]$
$v_9 = k_{cl,enz.domain,trans,p43}[DISC\_p55][p43]$	$v_{19} = k_{cl,probe}[Pr_{cpl}mCherry]$ $([p43] + [p18])$
$v_{10} = k_{cl,enz.domain,cis}[p30]$	

Table S3. Model equations of variants cis+trans/cis+trans and cis/trans.

differential equations 'cis+trans/cis+trans'		differential equations 'cis/trans'	
$\frac{d[CD95_{active}]}{dt} = -v_1 + v_2$	(1)	$\frac{d[CD95_{active}]}{dt} = -v_1 + v_2$	(1)
$\frac{d[FADD]}{dt} = -v_1 + v_2$	(2)	$\frac{d[FADD]}{dt} = -v_1 + v_2$	(2)
$\frac{d[p55]}{dt} = -v_3$	(3)	$\frac{d[p55]}{dt} = -v_3$	(3)
$\frac{d[DISC]}{dt} = v_1 - v_2 + v_{10} + v_{11} + v_{12} + v_{13} + v_{14} + v_{15}$	(4)	$\frac{d[DISC]}{dt} = v_1 - v_2 + v_{11} + v_{12} + v_{13}$	(4)
$\frac{d[DISC\_p55]}{dt} = v_3 - v_4 - v_5 - v_6 - v_7 - v_8 + v_9$	(5)	$\frac{d[DISC\_p55]}{dt} = v_3 - v_4 - v_8 + v_9$	(5)
$\frac{d[p30]}{dt} = v_4 + v_5 + v_6 - v_{10} - v_{11} - v_{12}$	(6)	$\frac{d[p30]}{dt} = v_4 - v_{11} - v_{12}$	(6)
$\frac{d[p43]}{dt} = v_7 + v_8 + v_9 - v_{13} - v_{14} - v_{15}$	(7)	$\frac{d[p43]}{dt} = v_8 + v_9 - v_{13}$	(7)
$\frac{d[p18]}{dt} = v_{10} + v_{11} + v_{12} + v_{13} + v_{14} + v_{15} - v_{16}$	(8)	$\frac{d[p18]}{dt} = v_{11} + v_{12} + v_{13} - v_{16}$	(8)
$\frac{d[tBID]}{dt} = v_{17}$	(9)	$\frac{d[tBID]}{dt} = v_{17}$	(9)
$\frac{d[Pr_{ER}]}{dt} = v_{18}$	(10)	$\frac{d[Pr_{ER}]}{dt} = v_{18}$	(10)
$\frac{d[Pr_{cpl}]}{dt} = v_{19}$	(11)	$\frac{d[Pr_{cpl}]}{dt} = v_{19}$	(11)

Table S4. Estimates of protein numbers in CD95R-HeLa and wild-type HeLa cells. The fusion proteins FADD-GFP, procaspase-8-GFP, and GFP-BID-mCherry were stably expressed in these two cell lines. By loading different amounts of recombinant GFP together with cell lysates containing the fusion proteins, the concentrations of the fusion proteins and the ER-anchored probe (Calnexin-GIETDS-GFP) were determined with an antibody against GFP. In a second step, the concentrations of FADD, procaspase-8, BID, and the cytosolic probe (NES-GIETDS-mCherry) were determined by loading different amounts of calibrated fusion proteins and immunostaining with antibodies against FADD, procaspase-8, BID, and mCherry. Thereby, rough estimates of protein numbers with large standard deviations were obtained and used as start values in the parameter-fitting procedures.

	CD95R-HeLa (mean ± SD)	**HeLa wt** (mean ± SD)
FADD	200843 ± 31549	229583 ± 31073
procaspase-8	334075 ± 143428	324431 ± 164643
BID	509926 ± 48462	571555 ± 108848
cytosolic probe	2093323 ± 759296	4852343 ± 1514532
ER probe	11137085 ± 4103493	8428324 ± 4495411

Table S5. Receptor number estimates. Cells were incubated with high amounts of antibodies against CD95R. Using calibration beads with five different numbers of epitopes that are recognized by fluorescently labeled secondary antibodies, fluorescence intensities measured by FACS could be related to receptor numbers. Cells that were incubated with the secondary but without the primary antibody served as a measure of the background fluorescence intensities. Rough estimates were obtained for probe-expressing cells. The measured intensities were at the upper limit of the intensity range of the calibration beads. Therefore, the calibration error was large in the probe-expressing cells. To initialize the parameter estimation, we used a receptor concentration start value between the measure amount for the native and the probe-expressing cells according to N ≈ 30000 receptors for probe-expressing wild-type HeLa cells and N ≈ 250000 receptors for probe-expressing CD95R-HeLa cells (see table S6). These values are consistent with earlier studies on these cell lines (24, 25).

	N (confidence intervals)
HeLa wt	12085 (11807, 12363)
CD95R-HeLa	157087 (155607, 158580)
HeLa wt, with probe expression	63425 (53014, 73892)
CD95R-HeLa, with probe expression	330269 (322410, 338155)

Table S6. Initial values and lower and upper limits for estimations of initial concentration. The values for CD95R correspond to estimates from FACS measurements, whereas the values for FADD, procaspase-8, and BID correspond to the median protein numbers obtained from calibrated Western blots. For CD95R, FADD, procaspase-8, and BID, 5% and the 95% percentiles were estimated by fitting lognormal distributions to FACS signals. For the cytosolic and the ER probes, initial values were determined by microscopic intensity measurements. Therefore, it was sufficient to allow large intervals for the estimation of initial concentrations of the cytosolic and the ER probes that were defined by the upper and lower limits shown in the table.

	CD95R-HeLa			**HeLa wt**		
	$\hat{c}$	$u_{5\%}$	$u_{95\%}$	$\hat{c}$	$u_{5\%}$	$u_{95\%}$
CD95R	116	34	396	12	2,4	58
FADD	93	21	405	90	22	372
procaspase-8	155	36	671	127	37	434
BID	236	59	943	224	47	1060
	$\hat{c}$	$c_{\min}$	$c_{\max}$	$\hat{c}$	$c_{\min}$	$c_{\max}$
cytosolic probe	973	100	5000	1909	200	10000
ER probe	5178	1000	10000	3316	1000	10000

Table S7. Cellular and cytosolic volumes, cell surface areas, and average fluorescence intensities. Measures of volumes, areas, and average fluorescence intensities for the cytosolic and the ER-anchored cleavage probes were obtained by segmentation from confocal microscopy image stacks. Median values, confidence intervals (c. i.) for the median estimates, and percentiles of the lognormal distributions are given in brackets. fl, femtoliters; A. U., arbitrary units

	CD95R-HeLa	**HeLa wt**
$\hat{V}_{cell}$ (c. i.) in fl	3585 (3457, 3717)	4236 (3903, 4597)
$(u_{5\%}, u_{95\%})$	(2554, 5031)	(2751, 6521)
$\hat{V}_{cpl}$ (c. i.) in fl	2515 (2413, 2622)	2980 (2722, 3263)
$(u_{5\%}, u_{95\%})$	(1705, 3711)	(1845, 4813)
$\hat{A}_{cell}$ (c. i.) in µm²	1475 (1424, 1527)	1404 (1314, 1501)
$(u_{5\%}, u_{95\%})$	(1063, 2046)	(988, 1995)
$\hat{I}_0(\mathrm{Pr}, cpl)$ (c. i.) in A.U.	54,46 (51.09, 58.05)	61.68 (58.41, 65.15)
$(u_{5\%}, u_{95\%})$	(29.95, 99.02)	(46.24, 82.29)
$\hat{I}_0(\mathrm{Pr}, ER)$ (c. i.) in A.U.	34.88 (33.77, 36.03)	22.21 (19.59, 25.17)
$(u_{5\%}, u_{95\%})$	(25.77, 47.21)	(11.46, 43.04)

Table S8. Parameters of the fitted cis/trans model. Values of the 1% best of n = 1000 fits to single-cell and Western blot data CD95-HeLa and wild-type HeLa cells were included for means and standard deviations.

parameter	value of best fit	mean ± σ
$k_{on,FADD}$ (1/min)	$8{,}12\cdot10^{-4}$	$2{,}76\cdot10^{-3}\pm1{,}75\cdot10^{-3}$ (±63,4%)
$k_{off,FADD}$ (1/min)	0,00567	$9{,}40\cdot10^{-3}\pm1{,}07\cdot10^{-2}$ (±114%)
$k_{on,p55}$ (1/min)	0,000492	$4{,}04\cdot10^{-4}\pm9{,}53\cdot10^{-5}$ (±23,6%)
$k_{cl,prodomain}$ (1/min)	0,0114	$0{,}0110\pm8{,}82\cdot10^{-4}$ (±8,01%)
$k_{cl,enz.domain,trans,p55}$ (nM/min)	$4{,}47\cdot10^{-4}$	$4{,}39\cdot10^{-4}\pm2{,}49\cdot10^{-4}$ (±56,7%)
$k_{cl,enz.domain,trans,p43}$ (nM/min)	0,00344	$0{,}00333\pm4{,}58\cdot10^{-4}$ (±13,7%)
$k_{p18,inactive}$ (1/min)	0,0950	0,0943±0,00694 (±7,36%)
$k_{cl,BID}$ (nM/min)	0,000529	$5{,}29\cdot10^{-4}\pm6{,}28\cdot10^{-5}$ (±11,9%)
$k_{cl,probe}$ (nM/min)	0,00152	$1{,}57\cdot10^{-3}\pm1{,}47\cdot10^{-4}$ (±9,35%)
$K_{D,R}$ (nM)	8,98	196±145 (±73,8%)
$K_{D,L}$ (nM)	15,4	55,2±26,1 (±47,2%)
$s_{caspase-8}$ (nM/min)	0,00149	$0{,}00153\pm1{,}46\cdot10^{-4}$ (±9,51%)
$s_{Pr,mCherry}$ (nM)	0,0173	$0{,}0144\pm2{,}12\cdot10^{-3}$ (±14,7%)
$s_{Pr,mGFP}$ (nM)	0,00350	$0{,}00350\pm4{,}24\cdot10^{-4}$ (±12,1%)

Additional Supplementary Materials

Caspase-8 model MatLab scripts. A zip file containing 12 ".m" files executable in MatLab. Each model variant has an ODE and a plot file. Model trajectories of the variants referred to in Fig. 3D can be plotted for three exemplary cells of the cell ensemble models. Filename Caspase8Model_MatlabScripts.zip

Caspase-8 model SBML files. A zip file containing 4 ".xml" files: C8variants_cis_trans_CD95HeLa.xml, a file with model definitions of the best-fit 'cis/trans' variant containing median initial concentrations of CD95-HeLa cells; C8variants_cis_trans_HeLawt.xml, model definitions of the 'cis/trans' variant containing median initial concentrations of wild-type HeLa cells; C8variants_cistrans_cistrans_CD95HeLa.xml, model definitions of the complete 'cis+trans/cis+trans' variant containing median initial concentrations of CD95-HeLa cells; C8variants_cistrans_cistrans_HeLawt.xml, model definitions of the complete 'cis+trans/cis+trans' variant containing median initial concentrations of wild-type HeLa cells. Filename Caspase8Model_SBMLfiles.zip.

Caspase-8 single-cell data. An Excel file with single-cell caspase-8 activities shown in fig. S3. Filename Caspase8SglCellData.xls